CLNS 00-1665
GUTPA/98-12-1
OHSTPY-HEP-T-99-021
UTCCP-P-78
hep-ph/0003130

Scaling of the B and D meson spectrum in lattice QCD

Joachim Hein*

Newman Laboratory of Nuclear Studies, Cornell University, Ithaca, NY 14853, USA

Sara Collins*, Christine T.H. Davies*

Dept. of Physics & Astronomy, University of Glasgow, Glasgow G12 8QQ, Scotland, UK

Arifa Ali Khan

Center for Computational Physics, University of Tsukuba, Ibaraki 305-8577, Japan

Harry Newton*

Dept. of Physics & Astronomy, University of Edinburgh, Edinburgh EH9 3JZ, Scotland, UK

Colin Morningstar

Physics Department, Florida International University, Miami, FL 33199, USA

Junko Shigemitsu

Physics Department, The Ohio State University, Columbus, OH 43210, USA

John Sloan†

Dept. of Physics & Astronomy, University of Kentucky, Lexington, KY 40506, USA

February 1, 2008

We give results for the B and the D meson spectrum using NRQCD on the lattice in the quenched approximation. The masses of radially and orbitally excited states are calculated as well as S-wave hyperfine and P-wave fine structure. Radially excited P-states are observed for the first time. Radial and orbital excitation energies match well to experiment, as does the strange-non-strange S-wave splitting. We compare the light and heavy quark mass dependence of various splittings to experiment. Our B-results cover a range in lattice spacings of more than a factor of two. Our D-results are from a single lattice spacing and we compare them to numbers in the literature from finer

*Member of the UKQCD collaboration

†Present address: Spatial Technologies, Boulder, CO, USA

lattices using other methods. We see no significant dependence of physical results on the lattice spacing.
PACS: 11.15.Ha 12.38.Gc 14.40.Lb 14.40.Nd

I. INTRODUCTION

Mesonic bound states consisting of a single heavy quark, b or c, and a light quark, u, d or s, as well as gluons, provide an interesting laboratory to study strong interactions. The typical momentum within such states is much lower than the mass of the heavy quark. This leads to a situation where the heavy quark becomes non-relativistic and the properties of the bound state are essentially determined by the light quark and the glue. At leading order the splittings within the spectrum become independent of the properties of the heavy quark, such as its mass m_Q and spin s_Q, so that orbital and radial excitation energies are expected to match between the B-system and the D-system. The resulting approximate $SU(2N_h)$ symmetry, with N_h denoting the number of heavy flavours, is usually referred to as *heavy quark symmetry*, see [1] and the references therein. At the next order, $1/m_Q$ effects give rise to fine structure in the spectrum, several times larger in the D-system than for the B, see e.g. [2] for a review.

The spectrum of B and D states is not yet well established experimentally [3] although several new results have been reported recently [4–8]. Here we study the spectrum theoretically and from first principles using lattice QCD. This will aid the experimental search for new states. In the case of well-established states it will provide a test for the theory and/or the systematic errors in our calculation. Of key interest are decay matrix elements for B-factory experiments. Knowing how well the spectrum has been obtained gives confidence that we understand how to simulate B and D mesons reliably. This is important for the analysis of systematic errors in matrix element determinations.

To formulate heavy b and c quarks on the lattice, a naïve discretisation is inappropriate since the lattice spacings currently available are not small compared to the Compton wave length of those quarks ($m_Q a > 1$). Presently there are two different formulations available to simulate heavy quarks, non-relativistic QCD (NRQCD) [9,10] and the heavy Wilson approach [11]. For the b-quark on present lattices both approaches become essentially the same. However, in this regime, NRQCD is to be preferred since the inclusion of higher order correction terms is easily implemented.

In this publication we report on our calculations of the B-meson spectrum for two different values of the lattice spacing a. Together with the results of [12], which were obtained with the same methods at another value of the lattice spacing, we can investigate the dependence on a of our results. Physical results must be independent of a and hence we can perform a test of systematic errors inherent in our calculation. We find no such errors at a significant level. In addition, on our coarsest lattice, we were able to simulate the D-meson spectrum

and compare to results using heavy Wilson methods on finer lattices (where NRQCD does not work well since $am_c < 1$). Early results on our coarse lattice have already been published in [13].

Section II gives details of the simulations we performed and section III gives details of our fit procedure. Section IV gives our determination of the bare b and c quark masses. Section V discusses the behaviour of the splittings in the spectrum that we obtain. This includes fits to the dependence of the splittings on the mass of the heavy quark. Section VI compares the results in physical units at different values of the lattice spacing and with previous results as well as with experiment. Readers interested in our results for the physical meson spectrum could jump directly to this section. Section VII contains our conclusions and our best estimate for the B-spectrum, based on the combined input from three different values of the lattice spacing.

II. SIMULATION DETAILS

A. Gauge field action

Our calculation was performed on two sets of gauge field configurations, which were generated using the Wilson gauge action

$$S_G = \beta \sum_{x,\mu<\nu} [1 - \tfrac{1}{3}\mathrm{Re}\,\mathrm{Tr}\,(U_{x,\nu}U_{x+\hat{\nu},\mu}U^+_{x+\hat{\mu},\nu}U^+_{x,\mu})]\,. \tag{1}$$

This action has lattice artifacts of $\mathcal{O}(a^2)$. For the bare gauge coupling β, we used 5.7 and 6.2. The lattice volumes and the number of configurations are given in table I. We will refer to these configurations by their respective β-values.

B. Light quark propagators

The light quark propagators have been generated with the use of the Sheikholeslami-Wohlert action, also known as the clover action [14],

$$S_L = a^4 \sum_x \Big[\bar{\psi}_x\psi_x + \kappa \sum_\mu \Big[\bar{\psi}_{x-\hat{\mu}}(\gamma_\mu - 1)U_{x-\hat{\mu},\mu}\psi_x - \bar{\psi}_{x+\hat{\mu}}(\gamma_\mu + 1)U^+_{x,\mu}\psi_x\Big] - a\tfrac{1}{2}ic_{sw}\kappa \sum_{\nu,\rho} \bar{\psi}_x F_{\nu\rho,x}\sigma_{\nu\rho}\psi_x\Big]\,. \tag{2}$$

On the configuration set with $\beta = 5.7$ the clover coefficient c_{sw} is set to its tadpole-improved tree level value $c_{sw} = 1.5667$, as determined from the 4th root of the plaquette [15]. This

reduces the lattice spacing artifacts in the light quark propagators to $\mathcal{O}(\alpha_s a, a^2)$. At $\beta = 6.2$ we used the non-perturbative determined value of $c_{sw} = 1.6138$, which removes the $\mathcal{O}(\alpha_s a)$ artifacts from the light quark propagator as well [16].

In reference [17] the light hadron spectrum at $\beta = 6.2$ has been calculated using the non-perturbative as well as the tadpole-improved tree level value for c_{sw}. No significant differences in the meson and baryon spectrum could be resolved between the two values of c_{sw}. From this we expect the difference between tadpole and non-perturbatively improved light quarks at $\beta = 6.2$ to be well covered by the size of the statistical errors in our case as well. This allows us to compare our $\beta = 6.2$ results to the tadpole-improved results at $\beta = 5.7$ and in reference [12].

For each value of β we used 3 different values for the hopping parameter κ. The actual values are detailed in table II. The table also contains the values of κ_c and κ_s from the UKQCD collaboration [17,18] used in our calculation. The use of these values is appropriate for the analysis in terms of chiral extrapolations and scale setting that we have done. We also carefully include systematic errors from different chiral extrapolations and associated uncertainties in setting the scale. A recent re-analysis by UKQCD of their light hadron spectrum [19] gives somewhat different values for κ_c and κ_s. Our errors encompass any changes this would produce in our physical results.

C. Heavy quark propagators

The typical momentum scale inside a heavy light meson such as a B or D meson is of the $\mathcal{O}(\Lambda_{\mathrm{QCD}})$, which is small compared to the mass of the heavy quark. Therefore the mass of the heavy quark m_Q represents an irrelevant scale for the dynamics of the mesonic bound state and it is possible to simulate these states on lattices with a lattice spacing larger than the Compton wavelength of the heavy quark.

In our simulation we use a non-relativistic expansion of the heavy quark Hamiltonian, which is known as NRQCD [9,10].

$$H = H_0 + \delta H\,, \tag{3a}$$

$$H_0 := -\frac{\mathbf{D}^2}{2m_Q}\,, \tag{3b}$$

$$\begin{aligned}\delta H := &-c_4\frac{g}{2m_Q}\boldsymbol{\sigma}\cdot\mathbf{B} + c_2\frac{ig}{8m_Q^2}(\mathbf{D}\cdot\mathbf{E} - \mathbf{E}\cdot\mathbf{D}) - c_3\frac{g}{8m_Q^2}\boldsymbol{\sigma}\cdot(\mathbf{D}\times\mathbf{E} - \mathbf{E}\times\mathbf{D}) \\ &-c_1\frac{(\mathbf{D}^2)^2}{8m_Q^3} + c_5 a^2\frac{\mathbf{D}^{(4)}}{24m_Q} - c_6 a\frac{(\mathbf{D}^2)^2}{16nm_Q^2}\,.\end{aligned} \tag{3c}$$

Please note that the rest mass term of H has been omitted, resulting in a shift of the Hamiltonian, which is discussed in section IV. In the case of a heavy-light meson the NRQCD expansion has to be organised in powers of $\Lambda_{\rm QCD}/m_Q$ [20]. Here this expansion is used up to $\mathcal{O}((\Lambda_{\rm QCD}/m_Q)^2)$. We also include the $\mathbf{p}^4$ term, which is believed to be the leading term in $\mathcal{O}((\Lambda_{\rm QCD}/m_Q)^3)$. The last two terms correct for discretisation errors from finite lattice spacing in respectively the spatial and temporal derivatives. n is a stability parameter used in the evolution equation (4). The matching coefficients $c_1, \ldots, c_6$ are set to their tadpole-improved tree level values [15].

With the Hamiltonian H and δH the propagator of the heavy quark can be obtained from a Schrödinger-type evolution equation

$$G_{t+1} = \left(1 - a\tfrac{1}{2}\delta H\right)\left(1 - a\tfrac{1}{2n}H_0\right)^n U_4^+ \left(1 - a\tfrac{1}{2n}H_0\right)^n \left(1 - a\tfrac{1}{2}\delta H\right) G_t \quad \text{for } t > 1\,, \tag{4a}$$

$$G_1 = \left(1 - a\tfrac{1}{2}\delta H\right)\left(1 - a\tfrac{1}{2n}H_0\right)^n U_4^+ \left(1 - a\tfrac{1}{2n}H_0\right)^n \left(1 - a\tfrac{1}{2}\delta H\right) \phi_x\,. \tag{4b}$$

With ϕ_x we denote the source smearing function used on the initial time slice. At $\beta = 5.7$ we use 20 different values for m_Q in the range $0.6 \le am_Q \le 20.0$ and at $\beta = 6.2$ we use 10 values in the range $1.1 \le am_Q \le 6.0$. Details, including the n values, are given in the tables III and IV. For each value of β we performed 3 different runs. At $\beta = 5.7$ we label them A, C and S; for $\beta = 6.2$ they are labeled H, N and P.

For the S-wave mesons at $\beta = 5.7$ we used up to three different smearing functions, $\phi_{G,0}$, $\phi_{G,1}$ and $\phi_{G,2}$, in the different runs. These are convolutions of Gaussian functions for the light and the heavy quark with radii as detailed in table V. The configurations were fixed to Coulomb gauge. A local sink will be denoted with ϕ_L. In most cases our final $\beta = 5.7$ results were obtained with both sink and source smearing.

For $\beta = 6.2$ we use smearing for the heavy quark propagators only. In run H at $\beta = 6.2$ we applied a hybrid procedure of Jacobi smearing [21] and fuzzing [22]. For runs N and P we fixed the configurations to Coulomb gauge. We used hydrogenic wave functions $\phi_{Hg,1}$, $\phi_{Hg,2}$ and $\phi_{He,1}$ for run N. The indices 'g' and 'e' denote wave functions of the ground and first excited state. The details are given in table VI. In the P run we used Gaussian smearing with two different radii, $ar_Q = 2.5$ and 5.0.

The spin operators applied to construct mesonic states with the correct quantum numbers are detailed in table 1 of reference [23].

D. Lattice spacing

In the quenched approximation one obtains different values for the lattice spacing, depending on the quantity it is determined from. This is expected to be caused by the strong coupling α_s running differently in the *real world* and the quenched theory.

We use the physical mass of the ρ-meson [3] to fix the lattice spacing. This procedure is justified from the typical gluon momentum in a B or D meson being of similar size to the momentum in a light meson such as the π and ρ. Since heavyonium states probe a higher physical scale these are not appropriate to fix the scale for a heavy-light system in the quenched approximation. Using the ρ-scale should take care of most of the quenching effects.

The determination of m_ρ is complicated by the chiral extrapolation required, see reference [24] for a review. At $\beta = 5.7$ we use the result of [18]. The result of the linear extrapolation in the light quark mass m_q is quoted as the central value and the deviation of the quadratic fit is treated as a systematic uncertainty. At $\beta = 6.2$ a linear extrapolation is reported in reference [17]. We treat the difference to the 3rd order extrapolation from [25] as a systematic uncertainty. The numbers are compiled in table VII. We use:

$$\beta = 5.7: \quad a^{-1} = 1.116(12)(^{+56}_{-0})\ \text{GeV}, \quad a = 0.1768(19)(^{+0}_{-88})\ \text{fm}, \tag{5a}$$

$$\beta = 6.2: \quad a^{-1} = 2.59(^{+6}_{-10})(^{+9}_{-0})\ \text{GeV}, \quad a = 0.0762(^{+29}_{-18})(^{26}_{-0})\ \text{fm}. \tag{5b}$$

For comparison, table VII also shows the lattice spacing as obtained from the string tension σ and the bottomonium splitting $\overline{\chi}_b - \Upsilon$. As a physical value for σ we choose a result obtained from a potential model fit to the charmonium spectrum [26]. The lattice numbers originate from [27,28]. These results are in agreement with the outcome of the m_ρ analysis. As explained above, the bottomonium system probes a different scale and the values obtained using it do not agree with the result from light spectroscopy [29].

III. FITTING TECHNIQUES

A. Parametrisations

At $\beta = 5.7$ we used several different smearings at source and sink. For hadron correlators with a local sink, we applied simultaneous vector fits, requiring the fitted mass(es) m_k to agree for all propagators:

$$\langle \phi_L(t)|\phi_i(0)\rangle = \sum_{k=1}^{n} A_{i,k} \exp(-m_k t)\,, \qquad 1 \le i \le m\,, \tag{6}$$

$$A_{i,k} = \langle \phi_L|\psi_k\rangle\langle\psi_k|\phi_i\rangle\,. \tag{7}$$

In the case of sink and source smearing, we used simultaneous matrix fits. In matrix fits, the fitted amplitudes are constrained in their relationship with each other as well:

$$\langle \phi_j(t)|\phi_i(0)\rangle = \sum_{k=1}^{n} B^*_{j,k} B_{i,k} \exp(-m_k t)\,, \qquad 1 \le j,i \le m\,, \tag{8}$$

$$B_{i,k} = \langle\psi_k|\phi_i\rangle\,. \tag{9}$$

The fitting techniques are described in more detail in reference [23]. We found matrix fits to be more precise with respect to statistical errors. Due to the omission of the rest mass in eq. (3) the fitted mass is shifted with respect to the bound state mass. We denote the result of the fit as the simulation mass, $m_{\rm sim}$. The determination of the shift will be discussed in section IV.

To extract mass splittings we applied two different procedures. One is to fit the masses as above, take their difference, and then calculate the error from the bootstrap or jackknife samples of the difference. With this procedure one can easily take advantage of using different smearings. In the case of a single smearing function, a ratio-fit provides an alternative [20]. For this one divides the bootstrap or jackknife samples of the two propagators and fits the outcome with an exponential ansatz. The mass shift cancels out of the difference in both procedures.

B. Pseudo-scalar and vector meson

On the $\beta = 5.7$ configurations the simulation masses for pseudo-scalar and vector mesons have been determined most accurately in run A. In this run we only used the smearing functions $\phi_{G,1}$ and $\phi_{G,2}$. We found the double exponential matrix fit with sink and source smearing to deliver the most precise result. For the fit range we choose the initial time slice $t_{\rm min}$ two time slices larger than the first time slice delivering a reasonable χ^2. In general we choose the number of dropped time slices multiplied by the number of propagators used for the fit to be larger than or equal to the number of fit parameters. The reason for this procedure is as follows. The first reasonable value of χ^2 is observed once the residual excitations are just masked by the statistical uncertainties, which allows for them to be still of similar size. Each excited data point can eat up one fit parameter. Dropping as many data points as fit parameters delivers a fit which is entirely dominated by statistical

fluctuations. The residual fit range dependence of those fits becomes negligible against the statistical uncertainties. We judge χ^2 values resulting in a $Q \geq 0.1$ as reasonable, where Q denotes the probability of a fit having an even higher value of χ^2. The final result is given in table VIII.

In run H at $\beta = 6.2$ we only had one smearing function available. We extracted the final results from single exponential fits to the propagators with source and sink smearing. Their fit results turned out to be more precise than the ones from using a local sink. The final fit range was determined such that we observed a reasonable χ^2 and achieved stability of the fitted result against variation of the fit range. The results are displayed in table IX.

In the run N we used hydrogenic wave functions of different radii. We generated smeared local and smeared smeared meson propagators. However no cross correlators, e.g. $\phi_{\mathrm{Hg},1}$ at sink and $\phi_{\mathrm{He},1}$ at source, were calculated. Hence eq. (8) was inapplicable and we had to use vector fits in the case of smearing at sink and source as well.

In double exponential vector fits to two smearing functions, we observed extremely low values of Q. We observed that this is connected to unfortunate statistical fluctuations on certain time slices. However the fit parameters turned out to be stable with respect to variations of the fit range. These fits will be discussed in subsection V B in more detail. To obtain a more precise result for the S-wave ground states, we resorted to single exponential fits to single propagators and compared the outcome for the different smearing functions. This is shown in figure 1 for the pseudo-scalar propagator at $am_Q = 2.5$. The octagons indicate the final result for each propagator, as determined from the Q-value after dropping two time slices. Within statistical errors all results are in reasonable agreement with each other. For the final result, which is also included in table IX, we choose the smeared-smeared $\phi_{\mathrm{Hg},1}$ propagator. In the end these deliver the more accurate hyperfine splitting, due to superior noise cancellation between the pseudo-scalar and the vector meson state.

In this context it is interesting to note that the propagators with local sink and $\phi_{\mathrm{Hg},2}$ source smearing plateau much later than the others, but the results are in agreement with those from other propagators.

For the S wave states in the run P we only had the Gaussian smearing at the source with radius $ar_0 = 2.5$ and local sink. Since these propagators plateau quite late, we used $t_{\mathrm{min}} = 16$ for the final result, the error bars are not competitive with those above. Since they are needed for the later analysis of the P states we include them as well in table IX.

To describe physical bound states involving light u and d quarks, the results of tables VIII and IX have to be extrapolated in the light quark hopping parameter. On both sets of configurations, the difference between the critical and normal hopping parameter is smaller

than the uncertainty we assigned to κ_c in table II [17] and we use κ_c in our extrapolations. The normal hopping parameter is the one for which the extrapolations deliver the physical m_π/m_ρ ratio.

Due to the high statistical accuracy we achieved at $\beta = 5.7$ in the pseudo-scalar case, a linear ansatz in $am_q := \frac{1}{2}(\frac{1}{\kappa} - \frac{1}{\kappa_c})$ in a full covariant fit to all three data points, results in a fit with $\chi^2/\text{d.o.f.} > 8/1$ for $am_Q < 10$. This corresponds to $Q < 0.004$. The resulting curves do not describe the data. We carefully checked whether this is caused by a residual fit range dependence and found all the fit parameters including the *would-be* strange to non-strange meson splitting to be stable against variation of the fit range. This was done for an initial time slice t_{min} in a range from 3 to 6.

We therefore extracted our final result from a linear spline to the points with highest and lowest m_q and use the deviation of a quadratic spline as a systematic uncertainty of the chiral extrapolation. An example for the extrapolation is given in figure 2. From the figure it is obvious that interpolations to extract the heavy-strange meson mass are insensitive to the different ansätze and we do not assign an uncertainty due to the different interpolations. However, in the case of the heavy strange meson, we are faced with the problem that κ_s is highly sensitive to the quantity it is determined from. Our central value is interpolated to the κ as determined from m_K/m_ρ, and the difference to the outcome for κ corresponding to m_ϕ/m_ρ is treated as an uncertainty of the quenched approximation. The results are presented in table X.

For $\beta = 6.2$ the statistical accuracy is not as high and our data are well described by linear extrapolations. The results are presented in table XI.

IV. HEAVY QUARK MASSES

A. Mass shift from dispersion relation

The omission of the rest mass term m_Q in the Hamiltonian eq. (3) causes most of the shift of the simulation mass m_{sim} with respect to the physical meson mass. The mass, m_{rel}, of the meson can be determined from the relativistic dispersion relation of the meson $E(\vec{p}) = \sqrt{m_{\text{rel}}^2 + \vec{p}^2}$, which gives

$$m_{\text{rel}} = \frac{\vec{p}^2 - [E(\vec{p}) - E(0)]^2}{2[E(\vec{p}) - E(0)]}\,. \tag{10}$$

Here $E(\vec{p})$ denotes the total energy of the meson. The mass shift Δ_{rel} is defined as the difference

$$\Delta_{\mathrm{rel}} := m_{\mathrm{rel}} - m_{\mathrm{sim}} \,. \tag{11}$$

This shift per heavy quark should be universal for all hadronic states simulated at the bare heavy quark mass m_Q.

In our calculation at $\beta = 5.7$ we determined the mass shift from the difference in energy of the pseudo-scalar meson propagators with $a|\vec{p}| = 0$ and $2\pi/12$. This was done in run C at $\kappa = 0.1400$ with source smearing $\phi_{G,1}$ and a local sink. At large values of m_Q, we found a single exponential fit to the ratio of the correlators to plateau much later than the fits to the individual propagators. This is reflected in a large fit range dependence of the jackknife difference of the masses of the individual fits, for time slices in which no plateau was observed in the ratio-fit. For our final result we choose a minimal t-value two time slices larger than the first t-value for which we obtained a decent χ^2 in a fit to the ratio of propagators. The final result is presented in table XII and figure 3.

We also tried simultaneous vector fits according to eq. (6) with two exponents. We used propagators with source smearing $\phi_{G,1}$ and $\phi_{G,2}$. The jackknifed difference of the fitted ground state mass is in agreement with the above procedure; however, the statistical uncertainties, especially for large values of m_Q, are larger.

For $\beta = 6.2$ we calculated the mass shift in heavy quarkonia, since the statistical precision for heavy-light correlators at finite momentum was not sufficient. In the following, mass shifts from heavy quarkonia will be denoted by Δ_H. We simulated the vector-meson for $a|\vec{p}| \leq 2\frac{2\pi}{24}$. The kinetic mass m_1 was obtained from fits to the dispersion relations:

$$E_{\mathrm{sim}}(\vec{p}) = m_0 + \frac{\vec{p}^2}{2m_1} - \frac{\vec{p}^4}{8m_2^3} \,, \tag{12a}$$

$$E_{\mathrm{sim}}(\vec{p}) = m_0 + \frac{\vec{p}^2}{2m_1} - \frac{\vec{p}^4}{8m_1^3} \,, \tag{12b}$$

$$E_{\mathrm{sim}}(\vec{p}) = m_0 + \frac{\vec{p}^2}{2m_1} \,, \tag{12c}$$

with parameters m_0, m_1 and m_2. $E_{\mathrm{sim}}(\vec{p})$ denotes the simulation energy as determined from the propagator falloff. In the case of $am_Q \leq 1.3$ we used the ansätze (12a) and (12b); for the three heavier m_Q-values, (12b) and (12c). All fits gave fit parameters which were consistent within half of the statistical error. To obtain the shifts required for heavy-light spectroscopy we subtracted the simulation mass of the quarkonium vector-meson and divided by two. The final results are displayed in table XIII and figure 3. It is interesting to compare to the result from reference [29] — $a\Delta_H = 1.29(2)$ obtained at $am_Q = 1.22$. Due to higher statistics, this result is much more precise. This value is included as a square into figure 3 and agrees well with the newer results.

B. Mass shift in perturbation theory

The mass shift Δ can also be calculated in lattice perturbation theory [30]:

$$\Delta_{\rm pert} = Z_m m_Q - E_0 \,. \tag{13}$$

Here Z_m denotes the renormalisation constant connecting the bare lattice mass m_Q with the pole mass and E_0 denotes the heavy quark self energy constant. In the perturbative expansion the 1-loop contributions from Z_m and E_0 cancel each other to a large extent and the direct perturbative expansion of $\Delta_{\rm pert}$ is much better behaved than either perturbative series on its own. The Lepage Mackenzie scale aq^* [15] has been determined separately for Δ and it is larger than for Z_m or for E_0. The coefficients for

$$\Delta_{\rm pert} = m_Q[1 + \alpha_s(aq^*) \cdot \Delta^{(1)}] \tag{14}$$

can be found in table XIV. We use the $\alpha_P(aq = 3.4)$ values as determined from the 1×1 Wilson loop [31] with 2-loop running in order to evolve to the respective aq^*. For the final mass shift we assign a relative uncertainty of $\alpha_s^2(aq^*)$. Since $\Delta^{(1)}$ is small, this is more conservative than the squared 1-loop contribution. The final results are displayed in table XII for $\beta = 5.7$ and table XIII for $\beta = 6.2$. For values of m_Q not included in table XIV we interpolated linearly between the nearby values, which is completely sufficient within the claimed accuracy. The results for $a\Delta$ from perturbation theory and the lattice simulation are compared in figure 3. Apart from possibly the low m_Q region at $\beta = 5.7$, the figure shows excellent agreement between the two ways of calculating the mass shift.

For $\beta = 5.7$ the stability parameter n differs in some cases between the perturbative results and the simulation. However for $am_Q = 4$, where perturbative results exist for $n = 1$ and 2, the effect of n is completely negligible: we obtain $\Delta_{\rm pert} = 3.88(22)$ vs $3.89(24)$. From a comparison of the simulation result of the runs A and C at $\beta = 5.7$ we can also obtain evidence of the effect of the different n on the simulation mass $m_{\rm sim}$. For $am_Q = 1.0$ and $\kappa = 0.1400$ we measure $am_{\rm sim,ps} = 0.6265(21)$ and $0.6248(21)$ for $n = 5$ and 6 respectively. This difference is again completely negligible against the uncertainty we assign to $a\Delta$, even if we enlarge it by a factor of 3 to allow for a larger effect between $n = 4$ and 5. The former n was used in the perturbation theory. Note also that this difference tends to be in the opposite direction to that in $a\Delta$ implying that the effect of n on the physical mass is reduced when compared to the shift.

Here it is interesting to note that physical mass differences like the hyperfine splitting $m_{\rm hpf} = m_{\rm sim,v} - m_{\rm sim,ps}$ are even less sensitive to n. At the above mass parameter of $am_Q = 1.0$ we measure $am_{\rm hpf} = 0.0833(20)$ for $n = 4$ and $0.0835(20)$ for $n = 5$.

In summary the differences in n between the different runs as well as the perturbative shifts can be neglected safely even at the high level of accuracy we achieved here. This leaves us with a discrepancy between $\Delta_{\rm pert}$ and $\Delta_{\rm rel}$ for our lowest m_Q-values, which is roughly twice as large as the uncertainty we assign to the perturbative result.

On the other hand for $\beta = 6.2$ we observe excellent agreement between the precise result of [29] with the perturbative calculation at the relatively low value $am_Q = 1.22$.

Given a value for the shift Δ and the simulation mass $m_{\rm sim}$ from tables VIII, IX, XII and XIII, we can now calculate absolute masses for all the states. We do this for the ground state vector and pseudo-scalar mesons, both to fix the quark mass, as described in the next subsection. Moreover, we use the meson mass rather than the quark mass to discuss the m_Q dependence, since it is more directly comparable to experiment. We frequently plot results against $1/m_{\rm sav}$, where $m_{\rm sav}$ is the spin-average of the ground state vector and pseudo-scalar mesons

$$m_{\rm sav} = \tfrac{1}{4}(3m_{\rm v} + m_{\rm ps})\,. \tag{15}$$

This is preferable to $m_{\rm ps}$ alone since the spin-averaging reduces the dependence on sub-leading spin-dependent terms.

C. Bare heavy quark mass

To determine the bare quark mass m_Q corresponding to the b and c-quark, we compared the mass of the spin-averaged S-wave meson denoted with an overbar, with the experimental result. We used 5313 MeV for the $\bar{B}$, 5405 MeV for the $\bar{B}_s$, 1973 MeV for the $\bar{D}$ and 2076 MeV for the $\bar{D}_s$ [3]. For the interpolations we used spline-fits to three neighbouring points. The fits were done quadratically in m_Q and $1/m_Q$ and no significant difference was observed between the two. From the strange and non-strange meson we obtained identical results for the quark masses:

$$am_b = 1.64(5)(^{+8}_{-5})(^{+0}_{-7})\,, \quad \beta = 6.2 \tag{16a}$$

$$am_b = 4.20(25)(5)(^{+0}_{-24})\,, \quad \beta = 5.7 \tag{16b}$$

$$am_c = 0.87(6)(3)(^{+0}_{-13})\,, \quad \beta = 5.7 \tag{16c}$$

The errors as indicated in the parentheses give the uncertainty arising from the mass shift and the statistical and systematic uncertainty of the a determination. The uncertainties associated with the simulation mass $m_{\rm sim}$ are completely negligible here. For m_b we used the perturbative shifts $\Delta_{\rm pert}$. Using $\Delta_{\rm H}$ at $\beta = 6.2$ delivers $am_b = 1.59(^{+14}_{-5})(^{+6}_{-3})(^{+0}_{-5})$ and

using $\Delta_{\rm rel}$ at $\beta = 5.7$ gives $am_b = 4.16(^{+53}_{-31})(7)(^{+0}_{-30})$, which is agreement with $\Delta_{\rm pert}$ but with larger error. For m_c we used the simulation result $\Delta_{\rm rel}$. Here $\Delta_{\rm pert}$ would give $am_c = 1.02(8)(2)(^{+0}_{-10})$. The deviation from the result eq. (16c) reflects the difference between the Δ-values at low am_Q discussed above.

This careful analysis to fix the bare heavy quark mass is particularly necessary for fine structure splittings in the spectrum to be discussed in the next section. These are very sensitive to the heavy quark mass, generally as $1/m_Q$. In addition, any errors in the heavy quark mass must be fed into errors in the fine structure splittings in order to avoid underestimating those errors.

The bare masses do not scale with the lattice spacing as expected, because they are unphysical. A better quantity to consider would be the mass in the $\overline{\rm MS}$-scheme. This will be discussed in a future publication [32].

V. MASS DEPENDENCE OF LEVEL SPLITTINGS

In this section we describe how the results for the level splittings are extracted from our data. The dependence of the different splittings on the light and heavy quark mass is also discussed.

A. Flavour dependent splittings

The mass difference between heavy-light states distinguished only by their strangeness survives into the static limit. Based on the ideas of heavy quark symmetry such splittings are expected to depend weakly on the mass of the heavy quark. If a spin-averaged combination is taken, the leading heavy quark mass dependence arises purely from the kinetic term in eq. (3b). The size of the slope in $1/m_{\rm sav}$ then gives information on the difference in $\langle p_b^2 \rangle$ for the b-quark in the strange and non-strange states.

We calculated this splitting from the ground state S-wave results for κ_s and κ_c. The result is highly sensitive to the reported uncertainties in the chiral extrapolation and the determination of the strange hopping parameter κ_s. At $\beta = 5.7$ we determine the statistical uncertainties in a jackknife procedure applied to the difference of the individual results and at $\beta = 6.2$ we use the bootstrap.

For $\beta = 5.7$ our statistical errors are very small and we consider additional systematic uncertainties for the chiral extrapolation and κ_s. For $\beta = 6.2$ the quality of our data is not as good and we give statistical errors only. Using the κ_s-value determined from the ϕ

would lead to a 9% increase of the result, which is small compared to our statistical errors. The results are displayed in tables XV and XVI. In figure 4 we plot the result for the spin-averaged splitting at $\beta = 5.7$ versus the inverse of m_{sav}, in order to display its heavy quark dependence.

The figure displays a clear increase of the splitting with decreasing heavy quark mass. To quantify the slope of this dependence we perform a linear fit of the splitting result versus $1/m_{sav}$. The result, converted into physical units, is detailed in table XXV. The slope corresponds to a $\langle p_b^2 \rangle$ difference of $\approx [0.25(3)\ \mathrm{GeV}]^2$, which is of the size of $\Lambda^2_{\overline{\mathrm{MS}}}$, as expected.

Because of the larger statistical uncertainties, we do not observe a significant slope at $\beta = 6.2$. The data can be fitted nicely to a constant.

A comparison of our results with the ones of [12] for the pseudo-scalar case is plotted in figure 5. In this plot we show the result for the strange quark as determined from the K/ρ mass ratio only. Due to the large error bars we do not include the results obtained at the larger values of m_Q for $\beta = 6.2$. Within the accuracy of around 12% in the case of $\beta = 6.2$ or better, no sign of scaling violations shows up in the plot. We also observe excellent agreement with the experimental result.

B. Radial excitations

In order to obtain a reasonably stable and long plateau for the radially excited S-states on the coarse lattice at $\beta = 5.7$ we applied triple exponential matrix fits to the three smearing functions $\phi_{G,0}$, $\phi_{G,1}$ and $\phi_{G,2}$. This was done for the run S for a single κ of 0.1400 only, which is approximately equal to the strange as determined from the K-meson. Since in reference [12] the dependence of the $2^1S_0 - 1^1S_0$ splitting on the light quark mass was found to be very small, a variation of less than 2% when fixing κ_s from the K or K^*-meson, we can ignore any mismatch in our κ vs κ_s compared to the statistical uncertainties. We therefore treat our result as the answer for this splitting with κ_s as determined from the K.

In figure 6 we show a typical example for the excellent stability of the simulation masses am_{sim} against variation of the starting point t_{min} of the fit range. The extent in t_{min} for which we can resolve the excited state is 5 time slices or 0.28 GeV^{-1}. The rate of its disappearance is set by the $2S - 1S$ splitting of 600 MeV.

In the figure the first good value of Q is observed for $t_{min} = 2$. To be safe with respect to residual excitations we quote the final result for a fit range starting at time slice 4, which is the procedure described in subsection III B. The peak in Q at $t_{min} = 5$ results from the

fit becoming insensitive to the third exponential at this point.

The results for all 6 heavy quark masses are given in table XVII. In figure 7 we plot the heavy quark mass dependence of the spin-averaged splitting. The result shows a clear increase as the heavy quark mass is reduced. In table XXV we detail fit results for the offset and slope of this splitting with respect to $1/m_{sav}$. From the assumption that the increase of the splitting with $1/m_{sav}$ is caused by the difference in the kinetic energy $p^2/2m_Q$ between ground and radially excited states, the fitted slope gives a $\langle p_b^2 \rangle$ difference of $\approx$ $[0.95(15)\ \mathrm{GeV}]^2$. This is of the size of a few times $\Lambda^2_{\overline{\mathrm{MS}}}$ as would be expected.

On our fine lattice, since no cross-correlators between the different smearings had been calculated, we used simultaneous vector fits in all cases. The differences between the smearings $\phi_{Hg,1}$, $\phi_{He,1}$ and $\phi_{Hg,1}$ turned out to be too small for simultaneous fits with three exponentials and we had to resort to fits using 2 exponentials. Again we choose the starting point t_{min} of the fit range as described in subsection III B. With this procedure it is possible to extract reliable information on the excited state, as can be verified from the tables of reference [23] for the case of Υ-spectroscopy. Using propagators with sink and source smearing in vector fits, leads to a suppression of the excited state contamination, which made it impossible to extract a signal for the excited state. Therefore we used propagators with smearing at the source and local sinks to extract the radially excited states.

As denoted earlier, the fits to these propagators are plagued by statistical fluctuations, which lead to quite large χ^2 and low Q values. However, the fits describe the data reasonably and the fitted parameters are stable against variation of t_{min}. This is shown in figure 8. For a fit range starting point $t_{min} \geq 5$ we obtain $Q > 1\%$, which is low compared to what we obtained in the other fits. However it is not that low, that the fit could be ruled out on statistical grounds. Together with the good stability of the fitted masses against variations of t_{min} as displayed on the right hand side of the figure, we believe that our signal is genuine. In this example we extract the final result from $t_{min} = 8$. The results for the radially excited S-wave for this lattice spacing are compiled in table XVIII.

C. Orbital excitations

Orbitally excited P-state mesons have been investigated at both of our lattice spacings. The possible states consist of four non-degenerate energy levels; total angular momentum $J = 0$ and 2 as well as two $J = 1$ states. In the heavy quark symmetry picture a jj coupled basis is appropriate. In the vicinity of the static limit, the $J = 2$ and the higher of the $J = 1$ states are close and separated from the $J = 0$ and lower $J = 1$. The former correspond

to a light quark total angular momentum of $j_l = \frac{3}{2}$, the latter of $j_l = \frac{1}{2}$. We use an LS coupled basis to study the states, but expect our $^1P_1$ and $^3P_1$ channels to mix, leading to the observation of the lower $J^P = 1^+$ state with both operators. We will denote the state corresponding to $j_l = \frac{3}{2}$ with a prime.

At $\beta = 5.7$ again we use one light hopping parameter, $\kappa = 0.1400$. As in the case of the radial excitations, we treat this as the value corresponding to the strange quark as determined from the K-meson and the simulations have been performed in the run S. We used the derivatives of the smearings $\phi_{G,0}$ and $\phi_{G,1}$ at source and sink. The final results were obtained from double exponential simultaneous matrix fits to both smearings and are listed in table XIX.

The selection of the fit range proved to be very delicate for this a-value. The statistical error grows rapidly when increasing t_{min}, since the signal to noise is exponentially related to the $P - S$ splitting [9,33]. We give an example in section V F, where the fine structure is discussed. For the lightest values of am_Q and correlators with $^3P_2$ wave operators in the T-representation we obtained small values of Q of a few permille. We include the corresponding mass values into the table for the sake of completeness and mark them in *italics*. However we disregard them in the further evaluation. The results are always in agreement with the ones obtained in the E-representation and we do not believe there is a serious problem with this, simply statistical fluctuations.

In the second to last column of table XIX we give the spin-averaged P-state result which we calculate as

$$m(P_{sav}) = \frac{1}{12}\left[1 \cdot m(^3P_0) + 3 \cdot m(^1P_1) + 3 \cdot m(^3P_1) + 5 \cdot m(^3P_2E)\right] . \qquad (17)$$

The result is also shown in figure 9. For comparison we include the experimental result for the $B^*_{sJ}(5850)$ resonance and the spin-average of the D_{s1} and D^*_{s2} [3]. The figure displays at most a mild heavy quark mass dependence. To quantify this, we report in table XXV on the offset and slope of this splitting in physical units. The slope is consistent with a $\langle p_b^2 \rangle$ difference of $\mathcal{O}(\Lambda^2_{QCD})$, but is also consistent with zero.

P-states were also investigated in the run P for $\beta = 6.2$. We choose $am_Q = 1.6$, directly corresponding to the b-quark in eq. (16a). For the light quarks we use the strange hopping parameter $\kappa = 0.1346$. Since the results on our coarse lattice depend only weakly on m_Q we take the outcome as the final answer for B_s.

In the simulations we used two different smeared sources together with local sinks. Again we used derivatives of Gaussian smearing functions. The masses were extracted from double exponential vector-fits to both propagators. We observe reasonable Q-values for all applied

operators and include all channels into the spin-average

$$m(P_{sav}) = \frac{1}{12}\left[1 \cdot m(^3P_0) + 3 \cdot m(^1P_1) + 3 \cdot m(^3P_1) + 2 \cdot m(^3P_2E) + 3 \cdot m(^3P_2T)\right] . \quad (18)$$

The results for the fitted masses are displayed in table XX. The splitting between the spin-averaged P and S waves is given in tables XXI and XXII.

D. Radially excited P-states

Having available 2 different smearing functions at both of our lattice spacings, it is possible to obtain information on the radially excited P-states as well. In figures 10 we show the dependence of the fitted masses of the spin-averages of the 1P and the 2P on the starting point t_{min} of the fit range for two different values of m_Q. The figure displays a clear signal for an excited state and reasonable stability with respect to variations of t_{min}. However the error grows rapidly with increasing t_{min}. The Q-values of the ^3P_2E-fit, which is the last of the individual states included in the spin-average to reach a plateau, are included in figure 17. Decent Q-values are observed for $t_{min} = 3$. Since this is a 6 parameter matrix fit to four propagators, we take our final result from $t_{min} = 5$. The results for the spin-averaged 2P-state are summarised in table XIX. We give the splitting to the spin-averaged 1S and 1P-states in table XXI. We do not observe a significant slope for the splitting with respect to $1/m_{sav}$.

For $\beta = 6.2$ we show the plateau in figure 11. Due to the finer lattice, the growth in the error with increasing t_{min} is smaller than before. For the mass parameters used here, an example of a Q-plot will be given in figure 18 below. Here the first decent Q is observed for $t_{min} = 2$. Since this is a vector fit to 2 propagators, we take our final results from $t_{min} = 6$. The result and splittings are included in tables XX and XXII.

As noted when discussing radially excited S-states, due to our conservative selection of the fit range, we expect residual excitations to be negligible within the quoted statistical errors.

E. Hyperfine splittings

The mass difference between a pseudo-scalar and a vector S-wave meson is caused by the spin of the heavy quark. This hyperfine splitting is expected to vanish in the limit of infinitely heavy quark mass.

On our $\beta = 5.7$ lattice we determined the hyperfine splitting m_{hpf} from the difference of the results in table VIII. A crucial ingredient in obtaining a small statistical error is to choose identical fitting ranges for both correlators. If one of them has a plateau at a larger value of t_{min} than the other, we took this larger value to obtain m_{hpf} from the difference of the fitted masses. The error in this procedure is estimated with a jackknife. The results are displayed in table XXIII.

The chiral extrapolation of the hyperfine splitting turned out to be less difficult than that for the simulation mass of the pseudo-scalar and vector mesons. The curvature seems to cancel out between them and we have been able to perform linear fits to extrapolate to the chiral limit. However, in order to be consistent, we assign a systematic uncertainty to the result. This uncertainty is obtained from the difference to the outcome of first extrapolating the individual mesons to the chiral limit and then determining the hyperfine splitting. In this case we use the quadratic extrapolations to the chiral limit to take a possible curvature into account.

In our chiral extrapolations of the hyperfine splitting we observe a negative slope with respect to the mass am_q of the light quark, which is illustrated in figure 12. The left hand side gives an example of our chiral extrapolations and the right hand side shows the slopes measured at each value of am_Q. In order to construct a physically meaningful quantity, the latter has been multiplied by the strange quark mass, such that we can compare with experimental results for the difference between the strange and non-strange hyperfine splittings.

For B-mesons the light quark dependence of the hyperfine splitting is not well resolved experimentally, because of large uncertainties in the B_s hyperfine splitting. For D-mesons the situation is much clearer and one observes an increase with the light quark mass. However the magnitude of the slope is largely dependent on whether you compare the D_s hyperfine splitting with the hyperfine splitting of the D^+ or the D^0. We expect this difference in the experimental results to be mainly due to QED-effects, since these come in with opposite signs in the D^+ and the D^0. Since the D_s is positively charged as well, QED effects should largely cancel when comparing the hyperfine splittings of the D_s and the D^+ and one obtains a positive slope for the D-meson from the experiment.

Comparing our data to the experimental results, one observes our hyperfine splittings to be too small. This will be discussed in more detail in section VI. With respect to the slope, the result at the D has clearly the wrong sign and its magnitude is approximately twice as large as that from the experiment. We did not observe this effect in our $\beta = 6.2$ results, neither was it observed in [12]. Both of these results did not achieve the high statistical

accuracy we have at $\beta = 5.7$ and also use values of the heavy quark mass at around the B or heavier. For those values of m_Q the light quark mass dependence at $\beta = 5.7$ is also not that significant.

A slope of similar sign and size has been observed in the calculations of [34,38], although the authors did not comment on this. Reference [34] used a highly improved gluonic action with NRQCD heavy quarks on even coarser lattices and [38] a heavy clover action for the heavy quarks on a finer lattice $\beta = 6.0$. A detailed comparison with these results will be given below in section VI. In this context it is interesting to note, the slope of the hyperfine splitting as a function of the quark mass turns out to be to small in light hadron spectroscopy as well [44].

The calculations listed above are performed in the quenched approximation, which could be a factor contributing to the wrong slope. In potential model language, which is not necessarily appropriate here, the hyperfine splitting is related to the square of the wave-function at the origin. This in turn depends on the light quark mass and is independent of m_Q as $m_Q \to \infty$. The wrong slope could then reflect the fact that the wave-function at the origin is not increasing rapidly enough as the light quark mass increases. This is natural in the quenched approximation as the potential at the origin is weakened by the coupling constant running too quickly to zero at short distance.

An alternative scenario is one in which the coefficients of the relevant terms in the action, here c_{sw} in the light quark action, effectively carry some quark mass dependence that has not been included, leading to an underestimate of the hyperfine splitting at large am_q. In this case the effect would disappear as a is reduced and this seems to be contradicted by results on finer lattices [38].

Another cause could be a problem in the chiral extrapolation itself. The experimental result for hyperfine splitting $J/\psi - \eta_c$ in the charmonium system is smaller than the hyperfine splitting for the D and D_s-mesons. If one considers charmonium as a D_c-meson, one has to conclude that there is a maximum of the hyperfine splitting as a function of the light quark mass for $m_q < m_c$. If this maximum is attained for $m_q < m_s$, our observation of a negative slope of the hyperfine for $m_q \approx m_s$ would be in agreement with nature. In this case extrapolations from the strange region to lighter u and d-quarks as well as the chiral limit would be impossible.

Our final results for the hyperfine splitting at κ_c and κ_s are given in table XXIII. In figure 13 we display the dependence of the hyperfine splitting on the spin-averaged heavy-light meson mass. A linear fit in m_{sav}^{-1} for the five heaviest m_{sav} values gives reasonable values of Q. In table XXV we give the numerical outcome of this fit for the strange and

non-strange hyperfine splittings. As expected from HQET the intercept always turns out to be zero within statistical errors.

In the H run for $\beta = 6.2$ we determine the hyperfine splitting from ratio-fits. In order to determine this without excited state contamination we use a fit interval for which both of the individual correlators have reached a plateau. As noted above, no significant dependence on the light quark mass was observed and we were able to fit the results to a constant with reasonable values of Q. The result is given in table XXIV.

In case of the N and P run we determined the hyperfine splitting from the jackknife difference of masses obtained from the pseudo-scalar and vector meson propagator. In the N run we compared the outcome for the different smearings available, for different values of the starting point t_{min} of the fit range. An example is shown in figure 15. The different smearing functions lead to compatible answers for the hyperfine splitting. We use the outcome from the propagators with sink and source smearing $\phi_{Hg,1}$ for our final result. In figure 16 we compare the outcome of the different runs at $\beta = 6.2$. Clearly the outcome from the run N is the most precise. The result for the physical B_s hyperfine splitting will be extracted from this results.

Having observed clear signals for the radially excited S-wave states on our coarse lattice, we also studied their hyperfine splittings. Unfortunately the statistical noise grows rapidly and we observe no clear signal for a non-zero splitting. Our results are given in figure 14, comparing the radially excited state hyperfine splitting to that of the ground state. Although we cannot give a value for the hyperfine splitting of the radially excited S-state, our results support the expectation that it should be equal to or smaller than the ground state splitting.

F. P-state fine structure

To extract the P-state fine structure we investigate the jackknife difference of the masses of the individual channels reported in tables XIX and XX. Because the statistical noise grows rapidly as t_{min} increased, this proved to be delicate. For $\beta = 5.7$ this is illustrated in figure 17. For the matrix-fit to the ^3P_2E propagators we observe a jump in Q for $t_{min} = 3$. However in the plot of the fit range dependence of the $^3P_2E - {}^3P_0$ splitting the statistical uncertainty doubles between $t_{min} = 3$ and 5. Therefore it is hard to tell whether there is a plateau or not.

We quote final results for $t_{min} = 5$, which corresponds to dropping 2 timeslices from the first reasonable Q-value. With this procedure we obtain a large statistical error and no significant splitting can be resolved. More aggressive fitting would have led to a result

compatible with zero but with a statistical error of ≈ 30 MeV. We give our final numbers in table XXI. For the splitting we used the same fit range for both channels, which leads to slight deviations from the direct difference of the results in table XIX.

For $\beta = 6.2$ the situation is easier, as shown in figure 18. The noise on the splitting does not grow as fast as on the coarse lattice, because the $P - S$ splitting is smaller in lattice units. We observe the first reasonable Q values for $t_{\rm min} = 3$. Since this is a 6 parameter fit to two propagators, we drop 3 time slices and quote the final result for $t_{\rm min} = 6$. The results are given in table XXII. Here we also quote results for the splitting of the $J = 1$ channels to the $J = 0$ state. We reiterate that no significance should be attached to any difference in the results between the ${}^3P_1$ and the ${}^1P_1$ operators.

VI. THE PHYSICAL MESON SPECTRUM

In this section we determine the physical B and D-meson spectrum and investigate scaling by comparing results at different values of the lattice spacing. We also compare with experimental results and other lattice calculations.

A. B-meson spectrum

At both of our lattice spacings we can simulate the b-quark directly. Here we discuss our results for the physical B-spectrum. Together with the findings of [12] we want to investigate the dependence of the individual splittings on the lattice spacing. The findings are compared both to the existing experimental results and lattice investigations performed by other groups within a similar framework using NRQCD [34,35].

The results of reference [34] are useful in that they work at a larger lattice spacing than we do here. There are a number of problems, however that make their results not directly comparable. For example, they do not use either smeared correlators or standard fitting techniques, and this will give rise to an unknown systematic error. In addition they do not see a difference between fixing the lattice spacing from m_ρ using the clover action and from the charmonium $1P - 1S$ splitting. This is clearly seen on finer lattices [17,18,36]. If this arises from overestimating a^{-1} from m_ρ because of discretisation errors, then this is another source of systematic error. In particular, this feeds into the fixing of the bare b or c quark mass and into hyperfine splittings. Their final result for the splitting does not take into account the effect of any of the uncertainties in the bare quark mass determination. This

is particularly important for the hyperfine splitting and causes their errors to be heavily underestimated.

The results of [35] overlap with, but are not as complete as ours.

Unfortunately there are no results for heavy clover fermions available that we can use. References [38,39] quote numbers for the B spectrum. The first reference still uses extrapolations from the lighter quark masses into the b-region. Reference [39] determines the bare b-quark mass from heavyonium, which is not suitable for the heavy clover approach at the lattice spacings used [40,41]. However we will later compare to their findings for the D-spectrum, since this problem is not so severe for charmonium at the lattice spacings used.

Results from taking the b-quark as a static source also exist for spin-independent and flavour splittings, which survive in the infinite mass limit, see for example [42]. However we restrict the discussion here to a comparison with results simulated at the physical b-quark mass directly.

In the following we denote spin-averaged states by an overline.

We summarise our results for the B-spectrum in the tables XXVI and XXVII. As an example of the splitting between a strange and a non-strange meson we discuss the difference of the pseudo-scalar $\mathsf{B_s} - \mathsf{B}$ splitting in figure 19. We observe no scaling violations between our results and the agreement with the experimental value is excellent.

The results from [35] given in figure 19 include the statistical errors only and are taken from their figure 15. In [35] additional uncertainties for the average of the results at the two finest lattices are mentioned in the text. The overall agreement with our results is good. They notice an upward jump, however, for their result on their finest lattice. Unfortunately our result from our finest lattice comes with large uncertainties so that we are unable to clarify whether there is any real effect here. Given the lack of scaling violations in the rest of the results, it seems unlikely to us. Table VII confirms that the scale from m_ρ used by us and the scale from σ used in [35] are very close. The mismatch of scales of $\approx 3\%$ can be neglected safely.

The results from [34] are also in agreement with ours. They use the $\mathsf{K^*/K}$ ratio to fix the strange quark mass. This reduces their results compared to that using the K/ρ ratio. Assuming a shift of 10 to 20 MeV from this would increase the agreement. This is the size of the effect we observe on our coarse lattice from fixing the strange from ϕ/ρ instead of the K.

Figure 20 shows the scaling of the radially excited $\mathsf{B_s}$-meson. As discussed in subsection V B already, the extraction of a result for our finest value of a turned out to be more problematic than anticipated, and we are left with quite large statistical uncertainties. How-

ever the final result is in good agreement with the result from our coarser lattice as well as the result of [12].

We also included a preliminary experimental result from the DELPHI collaboration for an admixture of the non-strange $B' - B$ and $B^{*\prime} - B^*$ splitting [4,5]. Assuming the hyperfine splitting of the two states to be of similar size, which our findings support, we observe reasonable agreement here. Table XXVI also contains results for the radial excitation energy of the vector state and the spin-averaged S-wave.

The orbital excitations are compared in figure 21. The lattice results for the spin-averaged strange P state scale very well. The magnitude agrees nicely with the $B^*_{sJ}(5850)$ resonance, which is expected to be an admixture of the two $j_l = \frac{3}{2}$ states.

Our results for the radially excited P-states are compared in figure 22. This is the first observation of a signal for these states in a lattice calculation. As the figure shows we get consistent results from the two different lattice spacings investigated. To the best of our knowledge radially excited P-states have not been observed yet experimentally.

The splittings discussed above are all essentially light quark quantities, which survive into the static limit. Their scaling or non-scaling says more about the light quark action than the heavy quark sector. The hyperfine splitting is of a different nature and from its scaling behaviour one can learn about how well the heavy quarks are being described on the lattice. We display this in figure 23. Our result for the strange hyperfine splitting together with the findings from [12] shows good scaling.

However the result is much smaller than the experimental value. Since the leading term in the hyperfine splitting arises from the $\boldsymbol{\sigma} \cdot \mathbf{B}$ term in the action, eq. (3c), the result for the splitting is sensitive to the coefficient c_4 and the inclusion of radiative corrections beyond tadpole improvement is required. Preliminary calculations [43] indicate that the inclusion of the 1-loop corrections would increase the hyperfine splittings on the order of 10% for the lattice spacings used. The quenched approximation might also play a rôle here, since in light spectroscopy the hyperfine splittings turn out to be too small as well, see [44] for a review. This effect increases with increasing quark mass. Unfortunately reference [37], which investigates the effect of the inclusion of two flavours of dynamical quarks on the B-meson, does not give any evidence for an increase of the $B^* - B$ splitting due to sea-quark vacuum polarisation effects.

From the experience [29] in Υ-spectroscopy using NRQCD, one could have expected to observe scaling violations in the hyperfine splitting. Using the same heavy quark Hamiltonian as we do, [29] reports an increase of 50% for the $\Upsilon - \eta_b$ splitting, within the range from $\beta = 5.7$ up to $\beta = 6.2$. The leading discretisation correction for the hyperfine splitting

is $\mathcal{O}((a p_{\mathrm{gluon}})^2)$ [10]. Typical gluon momenta for the Υ-system are ≈ 1 GeV, while for the B-system they are $\mathcal{O}(\Lambda_{\mathrm{QCD}})$. From this one expects reduced scaling violations of $\approx 10\%$ in the B-system for our range of lattice spacings. This is the same size as our uncertainties on the hyperfine splitting and therefore consistent with the fact that no scaling violations show up in figure 23.

Results from [35] are for the chirally extrapolated splitting $B^* - B$ with statistical errors only, taken from their figure 17. In the text, the authors quote a result for the strange hyperfine splitting from the average of the two finest lattices, which is 3 MeV higher than the same average for the non-strange hyperfine splitting. An upwards shift of 3 MeV increases the already excellent agreement even further.

The results of [34], on the other hand, exhibit a clear disagreement to our findings as well as the findings of [35]. We believe that this is because they have determined the bare b-quark mass am_b using heavyonium.

The fine structure of the P-states is the last topic of this section. Unfortunately we have not been able to resolve this clearly on our coarsest lattice. The situation is displayed in figure 24, for the three sublevels which were resolved at $\beta = 6.0$ and 6.2. To investigate whether there is evidence for scaling violations in the fine structure we calculate the jack-knifed difference of the highest and lowest state. This is shown in figure 25. The error bars turn out to be large and the figure is inconclusive. A more aggressive fit on the coarser lattice, as discussed in subsection V E would lead to the conclusion that scaling violations were seen, but we believe that further work is needed to resolve this question.

Our results for the B-meson spectrum, together with those of [12] do not show signs of residual lattice spacing dependence within the achieved accuracy. Therefore we can average the results for the different values of the lattice spacing a to obtain our final results on the quenched B-meson excitation spectrum. The averages were obtained in the following way, for each value of a we add the different uncertainties in quadrature to obtain a single value. Here we omitted those sources of uncertainty which are associated with the quenched approximation. These are the uncertainty arising from fixing the strange quark mass from different physical quantities and in the case of the results of [12] the additional uncertainty of the lattice spacing a associated with the physical quantity used to fix a. At this step we also symmetrised with respect to unsymmetric uncertainties. The central values have been obtained from fitting the results to a constant in an uncorrelated fit with the above described uncertainties. This puts more weight on the more precise results than a simple average.

Our analysis at the individual values of a does not include an uncertainty for the residual

effect of the lattice spacing. Our actions are improved to $\mathcal{O}(\alpha_s a, a^2)$. Therefore for each value of a we add the maximum of $\alpha_s a \Lambda_{QCD}$ and $a^2\Lambda_{QCD}^2$ in quadrature to the uncertainty used in the fit. We quote the smallest of these three so obtained uncertainties as our final uncertainty for the quenched B-meson spectrum. This way we quote an accuracy which is of the same size as the one we checked for scaling violations. Determining the final uncertainty from the χ^2 of the fit would reduce the uncertainty beyond this level. This procedure also ensures that residual lattice spacing artifacts are properly included if the achieved accuracy differs over the three individual results and the average is largely determined by the coarser lattices.

Our final result on the B-meson splitting spectrum in the quenched approximation is given in table XXVIII and figure 26.

The question of the effect of quenching on the spectrum goes beyond the scope of this paper. We refer the reader to [37]. There the effects of the inclusion of 2 flavours of dynamical quarks on the spectrum in NRQCD have been investigated and compared to the findings of [12]. No significant difference between the quenched and $n_f = 2$ results for the $1S$, $2S$ and $1P$-states was found. In particular, as mentioned earlier, no significant sea quark effects were seen in the $1S$-hyperfine splitting. Since our investigations confirm scaling in the quenched heavy-light spectrum the conclusions of [37] are unchanged.

B. D-meson spectrum

In this section we discuss the D-meson spectrum and compare our result to existing lattice results as well as to experiment.

The convergence of the NRQCD expansion is particularly important in the D-range, where the expansion parameter $\Lambda_{QCD}/m_Q \approx \frac{1}{4}$. Useful results on the question of the convergence are contained in [34]. There the authors study the complete NRQCD action to $\mathcal{O}((\Lambda_{QCD}/m_Q)^3)$. Here we include all terms up to $\mathcal{O}((\Lambda_{QCD}/m_Q)^2)$ and the relativistic correction to the kinetic energy in $\mathcal{O}((\Lambda_{QCD}/m_Q)^3)$. The authors of [34] calculate the heavy light kinetic masses using eq. (12c) and show that the difference arising from $\mathcal{O}((\Lambda_{QCD}/m_Q)^3)$-terms is consistent with the expectation that they are sub-sub-leading in a Λ_{QCD}/m_Q expansion. The changes to the spin-averaged meson mass that we use to fix the quark mass are dominated by the $\frac{p^4}{m_Q^3}$ relativistic correction that we include. From this we conclude that remaining $\mathcal{O}((\Lambda_{QCD}/m_Q)^3)$ and higher order terms in the NRQCD expansion would only change the physical masses by at most a few percent. This allows us to use the results of [34] to estimate the changes in the hyperfine splitting which would be produced

by these additional terms at fixed bare quark mass.

The authors of [34] find that the $\mathcal{O}((\Lambda_{\rm QCD}/m_Q)^2)$ terms produce an effect somewhat smaller than a $\Lambda_{\rm QCD}/m_Q$ expansion might suggest, since they affect the hyperfine splitting indirectly. The only spin-dependent term at $\mathcal{O}((\Lambda_{\rm QCD}/m_Q)^2)$ is a spin-orbit type interaction. At $\mathcal{O}((\Lambda_{\rm QCD}/m_Q)^3)$ most terms produce a change of a few percent, but the one which is directly related to the $\boldsymbol{\sigma}\cdot\mathbf{B}$-term: $\{\mathbf{D}^2, \boldsymbol{\sigma}\cdot\mathbf{B}\}$ reduces the hyperfine splitting at the charm by 20%. However when including the other operators of $\mathcal{O}((\Lambda_{\rm QCD}/m_Q)^3)$, the second largest effect comes from the $\boldsymbol{\sigma}\cdot(\mathbf{E}\times\mathbf{E}+\mathbf{B}\times\mathbf{B})$ operator, which is also spin-dependent and works in the opposite direction to the other one. The total effect of $\mathcal{O}((\Lambda_{\rm QCD}/m_Q)^3)$ is below 10%. This is of the size of the naïve expectation for the suppression with respect to the leading term and not at all inconsistent with good convergence of the NRQCD expansion. Since we do not include these terms, we conclude, that we may be overestimating the quenched lattice hyperfine splitting of the D-meson by 10%.

Our results on the D-meson spectrum are summarised in table XXIX and in figure 27. The overall agreement to the experimentally observed spectrum is good. We will now discuss the individual splittings in more detail. We also compare our results to the lattice studies of [34,38,39]. All of these results use the quenched approximation as well. The publications [38,39] apply the heavy clover approach [11], which has quite different systematic uncertainties from NRQCD for charm quarks.

The flavour dependent $D_s^{(*)}-D^{(*)}$ splittings are in good agreement with the experimental results. Here it is interesting to note that our results reflect the increase of ≈ 10 MeV from the B to the D-meson system, which can already be expected from the good agreement of the slope with the experimental outcome in table XXV.

In figure 28 we compare our result for the strange to non-strange spin-averaged splitting to other lattice calculations. In order not to disguise other possible effects, we excluded the uncertainty of the strange quark mass from the plot. The results from [34] use the K^*/K ratio to define the strange quark. This should shift the results downwards, compared to fixing κ_s from the K/ρ ratio as used for the other results. The implications have already been discussed in the previous sub-section VI A. The uncertainties again allow for an upwards shift of these results by 10 to 20 MeV. It should be noted that we combined the results for the hyperfine splittings and the pseudo-scalar $D_s - D$ splitting from [34] to obtain the spin-averaged splitting.

Because of different systematic uncertainties, it is particularly interesting to compare to the heavy clover results of [38]. The results obtained with the use of the m_ρ-scale, which is the same as what we use, agree very well with ours. This agreement is expected

since [38] uses the same light quark and gauge field action and this quantity is essentially determined by the light quarks and the gluon field. We conclude that the results for the flavour dependent $D_s - D$ splitting agree well between the different approaches and, within the accuracy achieved, agree well with the experimental result.

For radially excited $D_s^{(*)\prime}$-mesons no experimental results are known to us. However the DELPHI collaboration reports on the observation of the non-strange $D^{*\prime}$ [6]. This result is still awaiting confirmation by the OPAL and the CLEO collaboration and its interpretation is disputed on the ground of its small experimentally observed width [45,46]. The splitting between the DELPHI result and the D^* has a similar size to our $D_s^{*\prime} - D_s^*$ splitting. Reference [39] reports lattice results from the heavy-clover approach. From their plot we read $D_s' - D_s \approx 840(160)$ MeV, which is in agreement with our findings. However this includes what the authors call "*continuum*" extrapolation out of a regime where the expansion parameter $am_Q = \mathcal{O}(1)$ is not small. We would prefer to compare to the unextrapolated results at the individual values of a.

Experimentally the only well established charmed P-states in the particle data book [3] are those which are expected to correspond to the states of total light angular momentum $j_l = \frac{3}{2}$. Recently the CLEO collaboration [7,8] claimed the observation of the D_1 state corresponding to $j_l = \frac{1}{2}$. CLEO gives a preliminary result of $D_1 = 2461(^{+41}_{-34})(10)(32)$ MeV, which is slightly heavier but compatible in error bars to the $D_1' = 2425$ MeV [3][1]. Our lattice calculation delivers the mass of the lighter of the two states. We did not observe a signal for an excited state slightly heavier than this.

In table XXIX our result for the $\bar{D}_s(1P) - \bar{D}_s$ splitting is compared to the spin-average of the D_{s1}' and D_{s2}^*, the $j_l = \frac{3}{2}$ states. The agreement is reasonable. Reference [38] reports on the $D_{s1} - \bar{D}_s$ splitting from a lattice study with the heavy clover approach. A comparison to our result for this splitting is given in figure 29. When using the same scale obtained from m_ρ both lattice results agree very well with each other. The agreement with experiment is also good.

It should be noted however, that the experimental result included in figure 29 is not necessarily the same as ours. The experimental P-state corresponds to $j_l = \frac{3}{2}$. If the CLEO trend is confirmed and the D_1 is indeed heavier than the D_1' and the same holds for the D_{s1} states, then the lattice result also corresponds to $j_l = \frac{3}{2}$. If not the lattice result will correspond to $j_l = \frac{1}{2}$, but the two states will be so close, that any mismatch is well covered

[1] We quote the charge-average.

by the error bars.

Table XXIX contains our final result for the radially excited 2P-state. This is the first result for this state from a lattice simulation.

As in the B-system the hyperfine splittings are too small when compared to the experimental result. Whereas in the B-system they were too small by $\approx 40\%$, here they are low by $\approx 25\%$. This could reflect a more severe quenching error for B-mesons. B-mesons are somewhat smaller states than D mesons and probe slightly different scales. This is a sub-leading effect in a heavy quark symmetry picture, however. Alternatively, if the error comes from radiative corrections to the c_4 coefficient, that would need to increase with m_Q. That is seen by the authors of [43].

The large uncertainty of ≈ 20 MeV on our result arises from the chiral extrapolations used in the lattice spacing determination and the way in which this feeds into the fixing of the bare quark mass. Naively we expect a doubling of the relative error, because a larger value of a requires a smaller value of am_Q to deliver the same physical m_{sav}. This smaller value of am_Q gives a larger hyperfine splitting am_{hpf}. When converting to physical units it picks up the uncertainty of a for the second time. In fact a factor of four is seen because of the flattening of the relation between the mass shift Δ and bare heavy quark mass m_Q, see figure 3, as well as the steepening up of the hyperfine splitting curve for large values of m_{sav} in figure 13.

In figure 30 we compare our results to the results from [34] obtained in NRQCD. We choose their result in $\mathcal{O}((\Lambda_{QCD}/m_Q)^2)$ as most relevant for this comparison. The good agreement with our results is in fact misleading. They fix their c-quark mass from charmonium instead of the D. Fixing from the D would lead to a larger value of am_c and lower hyperfine splitting, see subsection IV C and reference [36].

It is interesting to compare the result for the hyperfine splitting between NRQCD and heavy clover quarks. This is also done in figure 30 for the D_s hyperfine splitting. The heavy clover results of [39] appear to be higher than our result. However this is a result of their higher choice of scale coming from J/ψ instead of from m_ρ. This is confirmed by the findings of [38]. Using a scale from m_ρ gives a result which agrees with ours, using a scale from J/ψ agrees with reference [39]. It should be noted that in [38] the bare quark mass is determined from the D, where as in [39] it is determined from charmonium. For the heavy clover approach at $\beta = 6.0$ these differences are negligible within statistical errors [47].

As discussed at the beginning of this subsection, the inclusion of the terms $\mathcal{O}((\Lambda_{QCD}/m_Q)^3)$ contributing to the hyperfine splitting would decrease our result by $\approx 10\%$. However the heavy clover approach requires similar correction terms in the Hamiltonian to

achieve this level of accuracy.

The agreement of the NRQCD and the heavy clover result for the spin-dependent hyperfine splitting is encouraging, since the systematic uncertainties are quite different. The light quark content plays only a minor rôle for the hyperfine splitting, which depends essentially only on the heavy quark Hamiltonian. In NRQCD the leading contribution to the hyperfine splitting comes from the $\boldsymbol{\sigma} \cdot \mathbf{B}$ term in the action, whereas for heavy clover this is split between the kinetic hopping term and the clover term $\sigma_{\nu\rho} F_{\nu\rho}$, with the latter becoming more important as the lattice spacing becomes coarser. Both these actions give rise to systematic errors in the hyperfine splitting from mass-dependent radiative corrections to coefficients and neglected higher order terms, each at the 10% level, so the differences could have been significantly larger than observed.

VII. DISCUSSION

We present an extensive study of the B and D-meson spectrum using NRQCD heavy quarks and clover light quarks in the quenched approximation.

Our results include the splitting between the strange and the non-strange meson, hyperfine splittings, radially and orbitally excited states. For the first time in a lattice calculation we obtained a result on radially excited P-wave states. For spin-independent splittings we observe good agreement with experimental results. However, our result for the spin-dependent hyperfine splitting turns out to be too low in comparison to experiment. This is a well known effect in quenched hadron spectroscopy. Furthermore, in the present calculation hyperfine splittings are also affected by the neglect of radiative corrections in the matching of lattice NRQCD to continuum QCD.

Using two different values of the lattice spacing in the B-spectrum together with the results of [12] allows for a detailed investigation of the residual lattice spacing dependence of our final results. No scaling violations are observed within the achieved accuracy. Of particular interest is the scaling of the $B_s^* - B_s$ splitting, which depends heavily on the properties of the heavy quark content of the theory. Here scaling violations could be ruled out with an accuracy of $\approx 10\%$. The P-fine structure has not been resolved for all values of the lattice spacings and further work is needed for this quantity.

Our results on the B-meson spectrum are summarised in table XXVIII and figure 26 together with the findings of [12]. In addition to the uncertainties considered in the analysis at the individual values of a, the quoted uncertainties also contain an estimate for the residual lattice spacing artifacts of $\mathcal{O}(\alpha_s a, a^2)$. The table gives our final results for the

B-meson spectrum in the quenched approximation.

Our final results on the D-meson spectrum are shown in table XXIX and figure 27 above. This is our final result for a lattice spacing of $a^{-1} \approx 1.1$ GeV and does not include an estimate of the residual lattice spacing artifacts of $\mathcal{O}(\alpha_s a, a^2)$. For the above value of a, this corresponds to 13%, which is of similar size to or smaller than the otherwise achieved accuracy.

We compared our results to lattice results of other collaborations obtained with NRQCD or in the heavy clover framework. In general we observe good agreement. Discrepancies which appear at first sight could be traced to underestimated errors in these other results or the use of different scales when converting the lattice results into physical units. The excellent agreement of our results with the results obtained in the heavy clover approach is noteworthy because of the different systematics of these approaches.

These results are the most complete lattice results on the B and D-meson spectrum to date.

Acknowledgements

We would like to acknowledge useful discussions with Peter Boyle and Peter Lepage.

J.H. was supported by a Marie Curie research fellowship by the European commission under ERB FMB ICT 961729, by PPARC and the National Science Foundation. S.C. acknowledges fellowships from the Royal Society of Edinburgh and the Alexander von Humboldt Stiftung. A.A.K. was supported by the Research for the Future Program of the Japanese Society for the Promotion of Science. J.Sh. would like to thank members of the theoretical physics group at the University of Glasgow for their hospitality during an extended visit. Support from an UK PPARC Visiting Fellowship PPA/V/S/1997/00666, is gratefully acknowledged.

This work was supported by the DOE under DE-FG02-91ER40690, PPARC under GR/L56343 and NATO under CRG/94259.

The gauge configurations at both values of β and the light quark propagators at $\beta = 6.2$ have been generously provided by the UKQCD-collaboration. The simulations at $\beta = 5.7$ have been performed at NERSC supported by DOE and the ones at $\beta = 6.2$ at EPCC in Edinburgh supported by PPARC.

[1] M. Neubert, Phys. Rept. **245** (1994) 259.

[2] C. Davies, in *Computing Particle Properties*, editors H. Gausterer, C.B. Lang, (Springer Verlag, Berlin, Heidelberg 1998), `hep-ph/9710394`.

[3] C. Caso, et al., Eur. Phys. J. **C3** (1998) 1-794.

[4] M. Feindt, O. Podobrin (DELPHI collaboration), contr. pa01-021 ICHEP'96 Warshaw, DELPHI 96-93 CONF 22;

[5] C. Weiser, in *Proceedings of the 28th International Conference on High Energy Physics*, editors Z. Ajduk, A.K. Worblewski, (World Scientific, Singapore 1997) page 531.

[6] P. Abreu, et al., (DELPHI Collaboration), Phys. Lett. **426B** (1998) 231.

[7] J. Rodriguez, (CLEO Collaboration), Preprint, `hep-ex/9901008 v2`.

[8] CLEO Collaboration, CLEO CONF 99-6.

[9] B.A. Thacker, G.P. Lepage, Phys. Rev. **D43** (1991) 196.

[10] G.P. Lepage, et al., Phys. Rev. **D46** (1992) 4052.

[11] A. El-Khadra, A. Kronfeld, P. Mackenzie, Phys. Rev. **D55** (1997) 3933.

[12] A. Ali Khan, et al., Preprint, `hep-lat/9912034`.

[13] J. Hein, et al., Nucl. Phys. B (Proc. Suppl.) 63 (1998) 347.

[14] B. Sheikholeslami, R. Wohlert, Nucl. Phys. **B259** (1985) 572.

[15] G.P. Lepage, P.B. Mackenzie, Phys. Rev. **D48** (1993) 2250.

[16] M. Lüscher, et al., Nucl. Phys. **B491** (1997) 323.

[17] P.A. Rowland (UKQCD collaboration), PhD thesis, University of Edinburgh, 1997.

[18] H. Shanahan, et al., Phys. Rev. **D55** (1997) 1548.

[19] K. Bowler, et al., Preprint, `hep-lat/9910022`.

[20] A. Ali Khan, et al., Phys. Rev. **D53** (1996) 6433.

[21] R.M. Baxter, et al., Phys. Rev. **D47** (1993) 5128.

[22] P. Lacock, et al., Phys. Rev. **D51** (1995) 6403.

[23] C.T.H. Davies, et al., Phys. Rev. **D50** (1994) 6963.

[24] R. Burkhalter, Nucl. Phys. B (Proc. Suppl.) 73 (1999) 3.

[25] M. Göckeler, et al., Phys. Rev. **D57** (1998) 5562.

[26] E. Eichten, et al., Phys. Rev. **D21** (1980) 203.

[27] R.G. Edwards, U.M. Heller, T.R. Klassen, Nucl. Phys. **B517** (1998) 377.

[28] M.J. Teper, Preprint, `hep-th/9812187`.

[29] C.T.H. Davies, et al., Phys. Rev. **D58** (1998) 054505.

[30] C. Morningstar, Phys. Rev. **D50** (1994) 5902.

[31] C.T.H. Davies, et al., Phys. Rev. **D56** (1997) 2755.

[32] J. Hein, et al., Preprint in preparation

[33] C.T.H. Davies, B.A. Thacker, Nucl. Phys. **B405** (1993) 593.

[34] R. Lewis, R.M. Woloshyn, Phys. Rev. **D58** (1998) 074506.

[35] K-I. Ishikawa, et al., (JLQCD collaboration), Phys. Rev. **D61** (2000) 074501.

[36] C.T.H. Davies, et al., Phys. Rev. **D52** (1995) 6519.

[37] S. Collins, et al., Phys. Rev. **D60** (1999) 074504.

[38] Peter Boyle (UKQCD collaboration), Nucl. Phys. B (Proc. Suppl.) 63 (1998) 314.

[39] P.B. Mackenzie, S. Ryan, J. Simone, Nucl. Phys. B (Proc. Suppl.) 63 (1998) 305.

[40] S. Collins, et al., Nucl. Phys. B (Proc. Suppl.) 47 (1996) 455.

[41] A. Kronfeld, Nucl. Phys. B (Proc. Suppl.) 53 (1997) 401.

[42] C. Michael, J. Peisa, Phys. Rev. **D58** (1998) 034506.

[43] H.D. Trottier, G.P. Lepage, Nucl. Phys. B (Proc. Suppl.) 63 (1998) 865.

[44] T. Yoshie, Nucl. Phys. B (Proc. Suppl.) 63 (1998) 3.

[45] D. Melikhow, O. Pene, Phys. Lett. **B446** (1999) 336.

[46] P.R. Page, Phys. Rev. **D60** (1999) 057501.

[47] Peter Boyle, private communication.

TABLE I. Simulation parameters of the gauge field configurations. For $\beta = 6.2$ there have been three different runs H, N and P with different numbers of configurations. All configurations are generously provided by the UKQCD collaboration.

β	volume	box size	# configurations
5.7	$12^3 \times 24$	2.1 fm	278
6.2	$24^3 \times 48$	1.8 fm	H: 68; N,P: 144

TABLE II. The hopping parameters used in the simulation are denoted by κ_1 to κ_3. The values of κ_c and κ_s are taken from [17,18]. For κ_s we give the results as determined from K, K^* and ϕ.

β	κ_1	κ_2	κ_3	κ_c	$\kappa_s(K)$	$\kappa_s(K^*)$	$\kappa_s(\phi)$
5.7	0.1380	0.1390	0.1400	0.1434(1)	0.1399(1)	0.1393(2)	0.1391(2)
6.2	0.1346	0.1351	0.1353	$0.13587(^{+2}_{-5})$	0.13466(7)	$0.13461(^{+9}_{-21})$	$0.13455(^{+10}_{-21})$

TABLE III. Bare heavy quark masses used in the different runs at $\beta = 5.7$. In the second, third and fourth line we give the stability parameter n used in the evolution equation (4) of the runs A, C and S.

am_Q	20.0	12.5	10.0	8.0	6.0	5.0	4.0	3.5	3.15	2.75	2.45	2.2	2.0	1.7	1.5	1.3	1.125	1.0	0.8	0.6
A	1	1	1	1	1	2	2	2	2	3	3	3	3	3	3	5	5	5	6	7
C	1	1	1	1	1	2	2	2	2	3	3	3	3	4	4	5	6	6	8	10
S	–	–	–	1	–	–	2	–	2	–	–	–	3	–	–	–	6	–	8	–

TABLE IV. Bare heavy quark masses and stability parameters n used in the runs H, N and P at $\beta = 6.2$.

am_Q	6.0	4.5	4.0	2.5	2.0	1.6	1.44	1.3	1.2	1.1
H	1	–	1	–	2	–	–	3	3	4
N	–	1	–	3	–	–	3	–	–	–
P	–	–	–	–	–	3	–	–	–	–

TABLE V. Smearing radii applied at $\beta = 5.7$ to the heavy quark Q and the light quark q.

	$\phi_{G,0}$	$\phi_{G,1}$	$\phi_{G,2}$
ar_Q	1.0	2.0	3.0
ar_q	local	local	3.0

TABLE VI. Smearing radii applied to the heavy quarks in the run N at $\beta = 6.2$. The subscript 'g' denotes a ground state hydrogenic wave function, the 'e' an excited state. Throughout this run we used local light quarks.

am_Q	$\phi_{Hg,1}$	$\phi_{He,1}$	$\phi_{Hg,2}$
4.5	$ar_0 = 5.0$	–	–
2.5	$ar_0 = 5.0$	–	$ar_0 = 8.0$
1.44	$ar_0 = 4.0$	$ar_0 = 4.0$	$ar_0 = 8.0$

TABLE VII. Determination of the inverse lattice spacing a^{-1} from the ρ-meson mass [3,17,18,25]. The first parenthesis gives the uncertainties arising from statistical fluctuations, the second the uncertainty resulting out of the chiral extrapolation. For comparison we also give the scales as obtained from the string tension σ [26–28] and the bottomonium $\overline{\chi}_b - \Upsilon$ splitting [3,29].

		$\beta = 5.7$		$\beta = 6.2$	
Quant.	phys. [MeV]	lattice	a^{-1} [GeV]	lattice	a^{-1} [GeV]
m_ρ	770.0(8)	$0.690(8)(^{+0}_{-35})$	$1.116(12)(^{+56}_{-0})$	$0.297(^{+12}_{-7})(^{+0}_{-10})$	$2.59(^{+6}_{-10})(^{+9}_{-0})$
$\sqrt{\sigma}$	$\approx$430	0.3879(39)	$\approx$1.10	0.1608(10)	$\approx$2.67
$\overline{\chi}_b - \Upsilon$	440	0.311(6)	1.41(4)(2)(5)	0.125(5)	3.52(14)(4)(0)

TABLE VIII. Fitted simulation masses for the ground state pseudo-scalar and vector mesons at $\beta = 5.7$ from run A. This table has been obtained from double exponential matrix fits to correlators with the smearing functions $\phi_{G,1}$ and $\phi_{G,2}$ at source and sink.

am_Q	$am_{sim,ps}$			$am_{sim,v}$		
	$\kappa = 0.1380$	$\kappa = 0.1390$	$\kappa = 0.1400$	$\kappa = 0.1380$	$\kappa = 0.1390$	$\kappa = 0.1400$
20.0	0.765(4)	0.745(4)	0.724(4)	0.771(4)	0.750(4)	0.730(4)
12.5	0.769(3)	0.748(3)	0.727(4)	0.778(3)	0.757(3)	0.736(4)
10.0	0.7715(28)	0.750(3)	0.728(4)	0.7823(28)	0.761(3)	0.740(4)
8.0	0.7733(26)	0.7518(28)	0.730(3)	0.7868(28)	0.765(3)	0.744(4)
6.0	0.7752(23)	0.7532(27)	0.731(3)	0.7929(26)	0.7712(28)	0.749(3)
5.0	0.7756(23)	0.7534(26)	0.7307(28)	0.7966(25)	0.7747(27)	0.753(3)
4.0	0.7753(22)	0.7526(23)	0.7296(27)	0.8009(23)	0.7787(26)	0.756(3)
3.5	0.7743(22)	0.7514(23)	0.7281(27)	0.8031(23)	0.7808(26)	0.7582(28)
3.15	0.7730(21)	0.7499(23)	0.7264(26)	0.8046(23)	0.7821(26)	0.7594(28)
2.75	0.7702(21)	0.7468(23)	0.7230(26)	0.8057(23)	0.7830(25)	0.7602(28)
2.45	0.7670(20)	0.7433(22)	0.7194(25)	0.8062(23)	0.7833(25)	0.7603(28)
2.2	0.7631(20)	0.7392(22)	0.7149(25)	0.8059(23)	0.7829(25)	0.7598(28)
2.0	0.7586(20)	0.7345(22)	0.7101(23)	0.8050(23)	0.7818(25)	0.7585(28)
1.7	0.7487(19)	0.7242(21)	0.6994(23)	0.8016(23)	0.7781(25)	0.7546(28)
1.5	0.7386(19)	0.7137(21)	0.6886(23)	0.7969(23)	0.7732(26)	0.749(3)
1.3	0.7210(19)	0.6957(20)	0.6702(22)	0.7864(23)	0.7625(26)	0.739(3)
1.125	0.7000(18)	0.6743(20)	0.6484(22)	0.7731(23)	0.7490(26)	0.725(3)
1.0	0.6788(18)	0.6528(19)	0.6265(21)	0.7587(23)	0.7343(27)	0.710(3)
0.8	0.6238(18)	0.5970(19)	0.5706(24)	0.7183(25)	0.6934(28)	0.668(3)
0.6	0.5267(20)	0.4989(21)	0.4709(23)	0.6445(28)	0.619(3)	0.593(4)

TABLE IX. Fitted simulation masses for the pseudo-scalar and vector meson at $\beta = 6.2$. The top section gives the results for run H, the middle one for N and in the bottom we give the result for run P. The results for the runs H and N have been obtained from propagators with source and sink smearing. In P we used source smearing with local sinks.

am_Q	$am_{sim,ps}$			$am_{sim,v}$		
	$\kappa = 0.1346$	$\kappa = 0.1351$	$\kappa = 0.1353$	$\kappa = 0.1346$	$\kappa = 0.1351$	$\kappa = 0.1353$
6.0	0.449(10)	0.438(12)	0.419(21)	0.460(13)	0.431(20)	0.415(24)
4.0	0.443(8)	0.425(10)	0.417(12)	0.447(11)	0.426(11)	0.417(14)
2.0	0.420(6)	0.405(8)	0.398(10)	0.430(7)	0.412(9)	0.404(12)
1.3	0.383(5)	0.365(6)	0.357(7)	0.397(6)	0.379(8)	0.371(9)
1.2	0.373(5)	0.355(5)	0.347(7)	0.388(5)	0.370(8)	0.361(9)
1.1	0.358(4)	0.341(5)	0.333(7)	0.374(5)	0.353(8)	0.342(10)
4.5	0.435(4)	—	—	0.440(4)	—	—
2.5	0.421(4)	—	—	0.429(4)	—	—
1.44	0.388(3)	—	—	0.400(3)	—	—
1.6	0.406(4)	—	—	0.419(4)	—	—

TABLE X. Chiral extrapolation at $\beta = 5.7$. The first parenthesis gives the statistical uncertainty, the second one the uncertainty in the respective hopping parameter and, in the case of κ_c, the third parenthesis gives the uncertainty arising from the chiral extrapolation.

am_Q	$am_{sim,ps}$		$am_{sim,v}$	
	κ_c	κ_s	κ_c	κ_s
20.00	$0.656(6)(2)(^{+0}_{-7})$	$0.726(4)(^{+17}_{-0})$	$0.663(6)(2)(^{+0}_{-6})$	$0.732(4)(^{+16}_{-0})$
12.50	$0.657(6)(2)(^{+0}_{-7})$	$0.729(4)(^{+17}_{-0})$	$0.667(6)(2)(^{+0}_{-6})$	$0.738(4)(^{+17}_{-0})$
10.00	$0.658(5)(2)(^{+0}_{-7})$	$0.731(4)(^{+17}_{-0})$	$0.670(5)(2)(^{+0}_{-6})$	$0.742(4)(^{+17}_{-0})$
8.00	$0.658(5)(2)(^{+0}_{-7})$	$0.732(3)(^{+18}_{-0})$	$0.673(5)(2)(^{+0}_{-6})$	$0.746(3)(^{+17}_{-0})$
6.00	$0.658(5)(2)(^{+0}_{-7})$	$0.733(3)(^{+18}_{-0})$	$0.678(5)(2)(^{+0}_{-5})$	$0.751(3)(^{+18}_{-0})$
5.00	$0.657(4)(2)(^{+0}_{-7})$	$0.7330(28)(^{+181}_{-0})$	$0.680(5)(2)(^{+0}_{-5})$	$0.755(3)(^{+18}_{-0})$
4.00	$0.655(4)(2)(^{+0}_{-7})$	$0.7319(27)(^{+184}_{-0})$	$0.683(4)(2)(^{+0}_{-5})$	$0.7586(29)(^{+179}_{-0})$
3.50	$0.652(4)(2)(^{+0}_{-6})$	$0.7304(26)(^{+187}_{-0})$	$0.685(4)(2)(^{+0}_{-5})$	$0.7605(28)(^{+180}_{-0})$
3.15	$0.650(4)(2)(^{+0}_{-6})$	$0.7287(25)(^{+188}_{-0})$	$0.685(4)(2)(^{+0}_{-4})$	$0.7617(28)(^{+181}_{-0})$
2.75	$0.646(4)(2)(^{+0}_{-6})$	$0.7254(25)(^{+190}_{-0})$	$0.686(4)(2)(^{+0}_{-4})$	$0.7625(28)(^{+183}_{-0})$
2.45	$0.641(4)(2)(^{+0}_{-6})$	$0.7218(24)(^{+192}_{-0})$	$0.685(4)(2)(^{+0}_{-4})$	$0.7626(28)(^{+184}_{-0})$
2.20	$0.636(4)(2)(^{+0}_{-6})$	$0.7174(24)(^{+194}_{-0})$	$0.684(4)(2)(^{+0}_{-4})$	$0.7621(28)(^{+185}_{-0})$
2.00	$0.631(3)(2)(^{+0}_{-6})$	$0.7126(23)(^{+195}_{-0})$	$0.683(4)(2)(^{+0}_{-4})$	$0.7609(28)(^{+186}_{-0})$
1.70	$0.619(3)(2)(^{+0}_{-5})$	$0.7019(23)(^{+198}_{-0})$	$0.678(4)(2)(^{+0}_{-4})$	$0.7569(28)(^{+189}_{-0})$
1.50	$0.607(3)(2)(^{+0}_{-5})$	$0.6911(22)(^{+201}_{-0})$	$0.672(4)(2)(^{+0}_{-4})$	$0.7519(29)(^{+190}_{-0})$
1.30	$0.587(3)(2)(^{+0}_{-5})$	$0.6728(22)(^{+204}_{-0})$	$0.660(5)(2)(^{+0}_{-4})$	$0.7409(29)(^{+192}_{-0})$
1.125	$0.564(3)(2)(^{+0}_{-5})$	$0.6510(21)(^{+207}_{-0})$	$0.645(5)(2)(^{+0}_{-4})$	$0.727(3)(^{+20}_{-0})$
1.00	$0.541(3)(2)(^{+0}_{-5})$	$0.6291(21)(^{+210}_{-0})$	$0.630(5)(2)(^{+0}_{-4})$	$0.712(3)(^{+20}_{-0})$
0.80	$0.483(3)(3)(^{+0}_{-5})$	$0.5733(23)(^{+215}_{-0})$	$0.590(5)(2)(^{+0}_{-3})$	$0.673(4)(^{+20}_{-0})$
0.60	$0.380(3)(3)(^{+0}_{-6})$	$0.4737(22)(^{+225}_{-0})$	$0.512(6)(3)(^{+0}_{-4})$	$0.597(4)(^{+20}_{-0})$

TABLE XI. Chiral extrapolation at $\beta = 6.2$. The parenthesis gives the statistical uncertainty. The results have been extrapolated to $\kappa_c = 0.135873$ and $\kappa_s = 0.13466$.

am_Q	$am_{sim,ps}$		$am_{sim,v}$	
	κ_c	κ_s	κ_c	κ_s
6.0	0.417(19)	0.448(10)	0.383(36)	0.453(13)
4.0	0.396(16)	0.439(8)	0.392(17)	0.444(9)
2.0	0.383(12)	0.419(6)	0.387(17)	0.429(6)
1.3	0.341(8)	0.381(5)	0.352(13)	0.395(6)
1.2	0.331(8)	0.371(5)	0.342(12)	0.384(6)
1.1	0.317(8)	0.357(5)	0.316(15)	0.370(5)

TABLE XII. Mass shift at $\beta = 5.7$.

am_Q	$a\Delta_{rel}$	$a\Delta_{pert}$
20.0	14.(5)	18.6(11)
12.5	9.3(20)	11.7(7)
10.0	7.9(13)	9.4(5)
8.0	6.7(9)	7.6(4)
6.0	5.4(6)	5.7(3)
5.0	4.6(4)	4.83(25)
4.0	3.96(26)	3.89(24)
3.5	3.52(22)	3.42(22)
3.15	3.20(19)	3.10(23)
2.75	2.85(16)	2.72(22)
2.45	2.57(14)	2.44(21)
2.2	2.34(12)	2.21(19)
2.0	2.16(11)	2.03(17)
1.7	1.89(9)	1.75(10)
1.5	1.68(6)	1.56(10)
1.3	1.51(6)	1.39(9)
1.125	1.37(5)	1.23(7)
1.0	1.27(5)	1.14(7)
0.8	1.16(4)	1.01(6)
0.6	1.13(4)	—

TABLE XIII. Mass shift at $\beta = 6.2$.

am_Q	$a\Delta_H$	$a\Delta_{pert}$
6.0	$5.5(^{+5}_{-6})$	5.82(16)
4.5	—	4.40(12)
4.0	$4.19(^{+22}_{-31})$	3.92(11)
2.5	—	2.49(9)
2.0	$2.26(^{+21}_{-26})$	2.02(8)
1.6	—	1.64(5)
1.44	—	1.49(4)
1.3	$1.28(^{+7}_{-13})$	1.36(4)
1.2	$1.17(^{+11}_{-12})$	1.27(4)
1.1	$1.07(^{+14}_{-20})$	1.18(3)

TABLE XIV. 1-loop coefficient and q^* of the perturbative expansion of the mass shift.

am_Q	n	$\Delta^{(1)}$	aq^*_Δ
20.00	1	−0.2968(66)	1.765(71)
12.50	1	−0.2605(46)	1.777(52)
10.00	1	−0.2446(35)	1.775(45)
7.00	1	−0.1987(37)	1.807(49)
5.00	1	−0.1522(34)	1.969(69)
4.00	1	−0.1227(27)	1.778(56)
4.00	2	−0.1115(23)	1.686(63)
3.50	2	−0.0889(23)	1.574(76)
3.00	2	−0.0538(21)	1.379(90)
2.70	2	−0.0308(20)	1.27(17)
2.50	2	−0.0104(23)	0.43(18)
2.00	2	0.0527(23)	1.25(28)
1.70	2	0.1109(25)	1.743(66)
1.60	2	0.1346(25)	1.639(53)
1.50	2	0.1615(24)	1.583(42)
1.40	3	0.2256(25)	1.858(38)
1.20	3	0.3276(26)	1.765(27)
1.00	4	0.5660(31)	1.793(20)
0.80	5	1.0915(42)	1.805(13)

TABLE XV. Splitting between the strange and non-strange meson at $\beta = 5.7$. The first parenthesis gives the statistical uncertainty, the second the effect of the different chiral extrapolations and the third the uncertainty arising from the κ_s determination.

am_Q	$a(m_{ps,s} - m_{ps})$	$a(m_{v,s} - m_v)$	$a(m_{sav,s} - m_{sav})$
20.000	$0.0697(26)(^{+73}_{-0})(^{+164}_{-0})$	$0.0691(27)(^{+63}_{-0})(^{+163}_{-0})$	$0.0693(27)(^{+63}_{-0})(^{+163}_{-0})$
12.500	$0.0717(23)(^{+76}_{-0})(^{+169}_{-0})$	$0.0709(23)(^{+61}_{-0})(^{+167}_{-0})$	$0.0711(24)(^{+62}_{-0})(^{+167}_{-0})$
10.000	$0.0727(21)(^{+76}_{-0})(^{+171}_{-0})$	$0.0717(22)(^{+61}_{-0})(^{+169}_{-0})$	$0.0720(22)(^{+62}_{-0})(^{+170}_{-0})$
8.000	$0.0736(20)(^{+76}_{-0})(^{+173}_{-0})$	$0.0725(20)(^{+60}_{-0})(^{+171}_{-0})$	$0.0728(20)(^{+61}_{-0})(^{+172}_{-0})$
6.000	$0.0749(18)(^{+74}_{-0})(^{+176}_{-0})$	$0.0736(19)(^{+57}_{-0})(^{+173}_{-0})$	$0.0739(19)(^{+58}_{-0})(^{+174}_{-0})$
5.000	$0.0758(18)(^{+72}_{-0})(^{+179}_{-0})$	$0.0742(18)(^{+54}_{-0})(^{+175}_{-0})$	$0.0746(18)(^{+56}_{-0})(^{+176}_{-0})$
4.000	$0.0770(16)(^{+70}_{-0})(^{+182}_{-0})$	$0.0751(18)(^{+50}_{-0})(^{+177}_{-0})$	$0.0756(18)(^{+53}_{-0})(^{+178}_{-0})$
3.500	$0.0779(16)(^{+69}_{-0})(^{+184}_{-0})$	$0.0757(18)(^{+48}_{-0})(^{+178}_{-0})$	$0.0762(17)(^{+51}_{-0})(^{+180}_{-0})$
3.150	$0.0786(15)(^{+67}_{-0})(^{+185}_{-0})$	$0.0761(17)(^{+46}_{-0})(^{+179}_{-0})$	$0.0767(17)(^{+49}_{-0})(^{+181}_{-0})$
2.750	$0.0795(15)(^{+65}_{-0})(^{+187}_{-0})$	$0.0767(17)(^{+44}_{-0})(^{+181}_{-0})$	$0.0774(17)(^{+47}_{-0})(^{+182}_{-0})$
2.450	$0.0803(14)(^{+63}_{-0})(^{+189}_{-0})$	$0.0773(18)(^{+42}_{-0})(^{+182}_{-0})$	$0.0780(17)(^{+45}_{-0})(^{+184}_{-0})$
2.200	$0.0811(14)(^{+61}_{-0})(^{+191}_{-0})$	$0.0778(18)(^{+41}_{-0})(^{+183}_{-0})$	$0.0786(17)(^{+44}_{-0})(^{+185}_{-0})$
2.000	$0.0818(13)(^{+59}_{-0})(^{+193}_{-0})$	$0.0783(18)(^{+41}_{-0})(^{+185}_{-0})$	$0.0792(17)(^{+43}_{-0})(^{+187}_{-0})$
1.700	$0.0831(13)(^{+57}_{-0})(^{+196}_{-0})$	$0.0792(18)(^{+40}_{-0})(^{+187}_{-0})$	$0.0802(17)(^{+42}_{-0})(^{+189}_{-0})$
1.500	$0.0842(12)(^{+56}_{-0})(^{+198}_{-0})$	$0.0800(19)(^{+40}_{-0})(^{+188}_{-0})$	$0.0810(17)(^{+42}_{-0})(^{+191}_{-0})$
1.300	$0.0855(12)(^{+56}_{-0})(^{+202}_{-0})$	$0.0808(19)(^{+41}_{-0})(^{+190}_{-0})$	$0.0819(17)(^{+42}_{-0})(^{+193}_{-0})$
1.125	$0.0869(12)(^{+56}_{-0})(^{+205}_{-0})$	$0.0817(19)(^{+42}_{-0})(^{+192}_{-0})$	$0.0830(17)(^{+44}_{-0})(^{+196}_{-0})$
1.000	$0.0882(11)(^{+57}_{-0})(^{+208}_{-0})$	$0.0824(20)(^{+44}_{-0})(^{+194}_{-0})$	$0.0839(17)(^{+45}_{-0})(^{+198}_{-0})$
0.800	$0.0903(12)(^{+55}_{-0})(^{+213}_{-0})$	$0.0827(22)(^{+31}_{-0})(^{+195}_{-0})$	$0.0846(19)(^{+35}_{-0})(^{+199}_{-0})$
0.600	$0.0940(12)(^{+63}_{-0})(^{+222}_{-0})$	$0.0851(24)(^{+38}_{-0})(^{+201}_{-0})$	$0.0874(20)(^{+42}_{-0})(^{+206}_{-0})$

TABLE XVI. Splitting between the strange and non-strange meson at $\beta = 6.2$. Results are quoted for κ_s determined from the K meson. Fixing κ_s from the ϕ would lead to an increase by 9%. The error bar gives the statistical uncertainty only.

am_Q	$a(m_{ps,s} - m_{ps})$	$a(m_{v,s} - m_v)$	$a(m_{sav,s} - m_{sav})$
6.0	0.031(17)	0.070(29)	0.049(22)
4.0	0.043(11)	0.052(18)	0.050(15)
2.0	0.036(8)	0.042(12)	0.041(10)
1.3	0.039(5)	0.042(10)	0.043(9)
1.2	0.040(5)	0.042(8)	0.043(7)
1.1	0.040(5)	0.055(12)	0.051(10)

TABLE XVII. Radially excited S-wave states at $\beta = 5.7$. These have been calculated in run S for $\kappa = 0.1400$.

am_Q	$am_{sim}(2S)$			$am_{sim}(2S) - am_{sim}(1S)$		
	ps	vector	spin-av	ps	vector	spin-av
8.0	1.148(27)	1.158(26)	1.155(26)	0.417(26)	0.412(25)	0.413(25)
4.0	1.21(4)	1.22(4)	1.22(4)	0.48(4)	0.46(4)	0.46(3)
3.15	1.23(4)	1.24(4)	1.24(4)	0.50(4)	0.48(4)	0.48(4)
2.0	1.26(5)	1.27(5)	1.26(5)	0.54(5)	0.51(5)	0.52(5)
1.125	1.23(9)	1.27(8)	1.26(8)	0.58(9)	0.55(8)	0.56(8)
0.8	1.17(12)	1.25(10)	1.23(10)	0.60(12)	0.58(9)	0.59(9)

TABLE XVIII. Radially excited S-wave states at $\beta = 6.2$. These have been calculated in run N for $\kappa = 0.1346$. These results are extracted from double exponential vector-fits to the smeared-local propagators with smearing functions as listed in the second column.

am_Q	smearing	$am_{sim}(2S)$			$am_{sim}(2S) - am_{sim}(1S)$		
		ps	vector	spin-av	ps	vector	spin-av
2.50	$\phi_{Hg,1}$, $\phi_{Hg,2}$	0.586(32)	0.586(36)	0.586(35)	0.154(34)	0.145(39)	0.147(37)
1.44	$\phi_{Hg,1}$, $\phi_{He,1}$	0.560(32)	0.565(34)	0.564(32)	0.165(33)	0.158(35)	0.160(34)

TABLE XIX. Simulation masses of the P-states at $\beta = 5.7$. These have been calculated in run S for $\kappa = 0.1400$. Values given in *italics* are obtained from fits with low values of Q and disregarded in the further analysis. Therefore the spin-average has been calculated according to eq. (17). The $^3P_1$ and $^1P_1$ operators should both yield the lightest physical $J^P = 1^+$ state.

am_Q	$am(1^3P_0)$	$am(1^1P_1)$	$am(1^3P_1)$	$am(1^3P_2E)$	$am(1^3P_2T)$	$am(1P_{sav})$	$am(2P_{sav})$
8.0	1.065(28)	1.071(26)	1.072(27)	1.13(8)	1.15(7)	1.09(7)	1.57(21)
4.0	1.088(27)	1.094(25)	1.097(26)	1.09(7)	1.13(7)	1.09(6)	1.64(20)
3.15	1.094(27)	1.103(26)	1.105(26)	1.08(7)	1.12(7)	1.09(6)	1.68(20)
2.0	1.097(27)	1.115(26)	1.116(26)	1.05(7)	*1.11(7)*	1.09(6)	1.74(22)
1.125	1.062(28)	1.100(26)	1.094(26)	1.01(8)	*1.09(7)*	1.07(6)	1.73(24)
0.8	0.995(29)	1.045(26)	1.034(25)	0.97(9)	*1.05(8)*	1.02(6)	1.64(24)

TABLE XX. Simulation masses of the P-states at $\beta = 6.2$. These have been calculated in run P for $\kappa = 0.1346$ and $am_Q = 1.6$. We report on the P-wave ground state and radially excited state. The spin-average has been calculated according to eq. (18).

$am(1^3P_0)$	$am(1^1P_1)$	$am(1^3P_1)$	$am(1^3P_2E)$	$am(1^3P_2T)$	$am(1P_{sav})$	$am(2P_{sav})$
0.521(17)	0.560(19)	0.553(20)	0.593(22)	0.588(23)	0.568(17)	0.90(8)

TABLE XXI. Splittings of the P-states at $\beta = 5.7$. These have been calculated in run S for $\kappa = 0.1400$.

am_Q	$am(1P-1S)_{sav}$	$am(2P-1S)_{sav}$	$am(2P-1P)_{sav}$	$am(^3P_2E-^3P_0)$
8.0	0.35(7)	0.83(22)	0.48(19)	0.12(10)
4.0	0.34(6)	0.90(20)	0.55(18)	0.03(8)
3.15	0.34(6)	0.93(20)	0.59(18)	0.00(8)
2.0	0.35(6)	0.99(22)	0.65(20)	−0.04(8)
1.125	0.36(5)	1.02(24)	0.66(21)	−0.07(8)
0.8	0.37(6)	1.00(23)	0.63(21)	−0.05(9)

TABLE XXII. Splittings of the P-states at $\beta = 6.2$. These have been calculated in run P for $\kappa = 0.1346$ and $am_Q = 1.6$.

$am(1P-1S)_{sav}$	$am(2P-1S)_{sav}$	$am(2P-1P)_{sav}$	$am(^1P_1-^3P_0)$	$am(^3P_1-^3P_0)$	$am(^3P_2-^3P_0)$
0.152(17)	0.49(8)	0.33(8)	0.039(18)	0.032(12)	0.069(25)

TABLE XXIII. The hyperfine splitting m_{hpf} at $\beta = 5.7$. The directly measured results are obtained from the difference of the results in table VIII. The results for κ_c and κ_s are extracted from linear fits to all three simulation results. The first parenthesis gives the statistical error. At κ_c the second parenthesis gives the uncertainty of the chiral extrapolation. We quote the strange results for κ_s from the K and the second parenthesis gives the deviation of the result for κ_s from the ϕ.

am_Q	am_{hpf} directly measured			am_{hpf} extrapolated/interpolated	
	$\kappa = 0.1380$	$\kappa = 0.1390$	$\kappa = 0.1400$	κ_c	κ_s
20.0	0.0054(3)	0.0056(4)	0.0058(4)	$0.0060(6)(^{+14}_{-0})$	$0.0057(4)(^{+0}_{-1})$
12.5	0.0087(4)	0.0089(5)	0.0092(5)	$0.0093(8)(^{+21}_{-0})$	$0.0090(5)(^{+0}_{-1})$
10.0	0.0108(5)	0.0110(5)	0.0114(6)	$0.0115(9)(^{+23}_{-0})$	0.0111(6)(0)
8.0	0.0135(5)	0.0137(6)	0.0141(7)	$0.0142(10)(^{+24}_{-0})$	$0.0138(7)(^{+0}_{-1})$
6.0	0.0177(6)	0.0180(6)	0.0185(8)	$0.0187(11)(^{+26}_{-0})$	$0.0181(7)(^{+0}_{-1})$
5.0	0.0210(6)	0.0213(7)	0.0219(8)	$0.0224(12)(^{+27}_{-0})$	$0.0216(8)(^{+0}_{-2})$
4.0	0.0256(7)	0.0261(8)	0.0268(9)	$0.0276(13)(^{+28}_{-0})$	$0.0265(9)(^{+0}_{-3})$
3.5	0.0288(8)	0.0294(8)	0.0301(10)	$0.0312(14)(^{+30}_{-0})$	$0.0298(10)(^{+0}_{-3})$
3.15	0.0316(8)	0.0322(9)	0.0330(10)	$0.0343(15)(^{+30}_{-0})$	$0.0327(10)(^{+0}_{-4})$
2.75	0.0355(8)	0.0363(10)	0.0372(11)	$0.0387(16)(^{+31}_{-0})$	$0.0368(11)(^{+0}_{-4})$
2.45	0.0392(9)	0.0400(10)	0.0410(12)	$0.0427(17)(^{+31}_{-0})$	$0.0406(11)(^{+0}_{-5})$
2.2	0.0429(9)	0.0437(11)	0.0448(13)	$0.0468(18)(^{+30}_{-0})$	$0.0444(12)(^{+0}_{-6})$
2.0	0.0464(10)	0.0473(11)	0.0484(13)	$0.0506(19)(^{+30}_{-0})$	$0.0480(12)(^{+0}_{-6})$
1.7	0.0529(11)	0.0539(12)	0.0552(15)	$0.0578(20)(^{+28}_{-0})$	$0.0547(13)(^{+0}_{-7})$
1.5	0.0584(11)	0.0595(13)	0.0609(16)	$0.0639(22)(^{+26}_{-0})$	$0.0604(14)(^{+0}_{-8})$
1.3	0.0655(12)	0.0668(14)	0.0683(17)	$0.0717(23)(^{+26}_{-0})$	$0.0678(16)(^{+0}_{-10})$
1.125	0.0731(14)	0.0746(16)	0.0763(19)	$0.0803(25)(^{+24}_{-0})$	$0.0758(17)(^{+0}_{-11})$
1.0	0.0799(15)	0.0816(17)	0.0833(20)	$0.0879(27)(^{+22}_{-0})$	$0.0828(19)(^{+0}_{-12})$
0.8	0.0945(17)	0.0965(20)	0.0998(25)	$0.106(3)(^{+4}_{-0})$	$0.0990(23)(^{+0}_{-15})$
0.6	0.1185(24)	0.1210(26)	0.124(3)	$0.131(4)(^{+4}_{-0})$	$0.1230(29)(^{+0}_{-18})$

TABLE XXIV. The hyperfine splitting m_{hpf} at $\beta = 6.2$. The results are obtained from ratio-fits to the propagators with source and sink smearing. The parenthesis gives the statistical uncertainty.

am_Q	$\kappa = 0.1346$	$\kappa = 0.1351$	$\kappa = 0.1353$
6.0	−0.0016(22)	−0.0026(30)	−0.004(4)
4.0	0.0026(23)	0.0024(30)	0.0024(33)
2.0	0.0077(25)	0.0072(32)	0.007(4)
1.3	0.0130(24)	0.0121(36)	0.012(4)
1.2	0.0141(24)	0.0132(36)	0.013(4)
1.1	0.0154(24)	0.0146(36)	0.014(4)
4.5	0.0040(5)	—	—
2.5	0.0070(7)	—	—
1.44	0.0120(8)	—	—
1.6	0.0123(18)	—	—

TABLE XXV. Dependence of the splittings Δm on the spin-averaged meson mass for $\beta = 5.7$. We report the constant and linear coefficient of the dependence on $1/m_{sav}$. For the strange splittings, the number in parenthesis give the statistical error, the uncertainty from the chiral extrapolation, the value of κ_s and the systematic uncertainty of the a-value. The last column reports the *experimental* slope from the difference of the splitting in the B and D system. Here we used the spin-average of the $j_l = \frac{3}{2}$ states for the P-state. Uncertainties which do not apply or have not been evaluated for reasons detailed in the text, are marked with (–).

Splitting	lattice		experiment
	$\Delta m(m_{sav}^{-1} = 0)$ in GeV	$\frac{\partial(\Delta m)}{\partial m_{sav}^{-1}}\|_{m_{sav}^{-1}=0}$ in GeV^2	$\frac{\partial(\Delta m)}{\partial m_{sav}^{-1}}$ in GeV^2
$m_{ps,s} - m_{ps}$	$0.079(3)(^{+7}_{-0})(^{+19}_{-0})(^{+4}_{-0})$	$0.037(7)(-)(^{+9}_{-0})(^{+4}_{-0})$	0.028(7)
$m_{v,s} - m_v$	$0.078(3)(^{+6}_{-0})(^{+19}_{-0})(^{+4}_{-0})$	$0.027(8)(-)(^{+6}_{-0})(^{+3}_{-0})$	0.035(12)
$m_{sav,s} - m_{sav}$	$0.079(3)(^{+6}_{-0})(^{+19}_{-0})(^{+4}_{-0})$	$0.029(8)(-)(^{+7}_{-0})(^{+3}_{-0})$	0.033(9)
$m_{ps,s}(2S) - m_{ps,s}(1S)$	$0.40(3)(-)(-)(^{+2}_{-0})$	$0.57(16)(-)(-)(^{+6}_{-0})$	—
$m_{v,s}(2S) - m_{v,s}(1S)$	$0.40(3)(-)(-)(^{+2}_{-0})$	$0.42(16)(-)(-)(^{+4}_{-0})$	—
$m_{sav,s}(2S) - m_{sav,s}(1S)$	$0.40(3)(-)(-)(^{+2}_{-0})$	$0.45(15)(-)(-)(^{+5}_{-0})$	—
$m_{sav,s}(1P) - m_{sav,s}(1S)$	$0.36(8)(-)(-)(^{+2}_{-0})$	$0.07(12)(-)(-)(^{+1}_{-0})$	0.11(5)
$m_v - m_{ps}$	$-0.0001(7)(^{+5}_{-0})(-)(0)$	$0.151(10)(^{+16}_{-0})(-)(^{+16}_{-0})$	0.297(1)
$m_{v,s} - m_{ps,s}$	$-0.0002(4)(-)(0)(0)$	$0.144(6)(-)(^{+0}_{-2})(^{+15}_{-0})$	0.304(17)

TABLE XXVI. Meson masses and splittings in the B system for $\beta = 5.7$. Overlines denote spin-averaged states.

Splitting	Value	Uncertainties						Experiment
		stat	chiral	strange	shift	a-stat	a-chiral	
$B_s - B$	85.6 MeV	(20)	$(^{+78}_{-0})$	$(^{+202}_{-0})$	(3)	(9)	$(^{+46}_{-0})$	90.2(22) MeV
$B_s^* - B^*$	83.6 MeV	(20)	$(^{+56}_{-0})$	$(^{+198}_{-0})$	(2)	(9)	$(^{+44}_{-0})$	91.4(38) MeV
$\bar{B}_s - \bar{B}$	84.1 MeV	(20)	$(^{+59}_{-0})$	$(^{+200}_{-0})$	(2)	(9)	$(^{+45}_{-0})$	91.(3) MeV
$B^{(*)}(2S) - B^{(*)}(1S)$	—	—	—	—	—	—	—	580.(10) MeV [4,5]
$B_s(2S) - B_s(1S)$	526. MeV	(38)	—	—	(7)	(7)	$(^{+34}_{-0})$	—
$B_s^*(2S) - B_s^*(1S)$	509. MeV	(38)	—	—	(6)	(7)	$(^{+32}_{-0})$	—
$\bar{B}_s(2S) - \bar{B}_s(1S)$	513. MeV	(37)	—	—	(6)	(7)	$(^{+33}_{-0})$	—
$B_{sJ}^*(5850) - \bar{B}_s(1S)$	—	—	—	—	—	—	—	448.(15) MeV
$\bar{B}_s(1P) - \bar{B}_s(1S)$	385. MeV	(70)	—	—	(0)	(4)	$(^{+19}_{-0})$	—
$\bar{B}_s(2P) - \bar{B}_s(1P)$	610. MeV	(200)	—	—	(9)	(6)	$(^{+40}_{-0})$	—
$B^* - B$	29.5 MeV	(15)	$(^{+31}_{-0})$	—	(16)	(6)	$(^{+31}_{-0})$	45.78(35) MeV
$B_s^* - B_s$	28.3 MeV	(10)	—	$(^{+0}_{-3})$	(15)	(6)	$(^{+30}_{-0})$	47.0(26) MeV
$B_{s2}^* - B_{s0}^*$	41. MeV	(94)	—	—	(11)	(3)	$(^{+14}_{-0})$	—

TABLE XXVII. Meson masses and splittings in the B system for $\beta = 6.2$. The radially excited S-wave states are extracted from fits with low Q-values compared to the other results. We quote them in italics.

Splitting	Value	Uncertainties					Experiment
		stat	strange	shift	a-stat	a-chiral	
$B_s - B$	96. MeV	(17)	$(^{+9}_{-0})$	—	$(^{+3}_{-4})$	$(^{+4}_{-0})$	90.2(22) MeV
$B_s^* - B^*$	109. MeV	(26)	$(^{+10}_{-0})$	—	$(^{+3}_{-4})$	$(^{+4}_{-0})$	91.4(38) MeV
$\bar{B}_s - \bar{B}$	109. MeV	(23)	$(^{+10}_{-0})$	—	$(^{+3}_{-5})$	$(^{+4}_{-0})$	91.(3) MeV
$B^{(*)}(2S) - B^{(*)}(1S)$	—	—	—	—	—	—	580.(10) MeV [4,5]
$B_s(2S) - B_s(1S)$	*420.* MeV	(85)	—	(3)	$(^{+12}_{-20})$	$(^{+17}_{-0})$	—
$B_s^*(2S) - B_s^*(1S)$	*400.* MeV	(90)	—	(3)	$(^{+12}_{-20})$	$(^{+17}_{-0})$	—
$\bar{B}_s(2S) - \bar{B}_s(1S)$	*405.* MeV	(90)	—	(3)	$(^{+12}_{-20})$	$(^{+17}_{-0})$	—
$B_{sJ}^*(5850) - \bar{B}_s(1S)$	—	—	—	—	—	—	448.(15) MeV
$\bar{B}_s(1P) - \bar{B}_s(1S)$	395. MeV	(45)	—	—	$(^{+9}_{-15})$	$(^{+14}_{-0})$	—
$\bar{B}_s(2P) - \bar{B}_s(1P)$	855. MeV	(210)	—	—	$(^{+20}_{-33})$	$(^{+30}_{-0})$	—
$B_s^* - B_s$	27.3 MeV	(20)	—	(8)	$(^{+15}_{-22})$	$(^{+22}_{-0})$	47.0(26) MeV
$B_{s2}^* - B_{s0}^*$	179. MeV	(65)	—	—	$(^{+4}_{-7})$	$(^{+6}_{-0})$	—

TABLE XXVIII. Summary of the results on the B-meson spectrum. The table gives the average of our results and the result of [12]. Errors exclude quenching effects but include residual lattice spacing artifacts of $\mathcal{O}(\alpha_s a, a^2)$. Again overlines denote spin-averaged states.

Splitting	Value	Experiment
$B_s - B$	90.(10) MeV	90.2(22) MeV
$B_s^* - B^*$	90.(10) MeV	91.4(38) MeV
$\bar{B}_s - \bar{B}$	90.(10) MeV	91.(3) MeV
$B^{(*)}(2S) - B^{(*)}(1S)$	—	580.(10) MeV [4,5]
$B(2S) - B(1S)$	600.(90) MeV	—
$B_s(2S) - B_s(1S)$	540.(60) MeV	—
$B_s^*(2S) - B_s^*(1S)$	525.(80) MeV	—
$\bar{B}_s(2S) - \bar{B}_s(1S)$	530.(80) MeV	—
$B_J^*(5732) - \bar{B}(1S)$	—	385.(12) MeV
$\bar{B}(1P) - \bar{B}(1S)$	455.(50) MeV	—
$B_{sJ}^*(5850) - \bar{B}_s(1S)$	—	448.(15) MeV
$\bar{B}_s(1P) - \bar{B}_s(1S)$	411.(45) MeV	—
$\bar{B}_s(2P) - \bar{B}_s(1P)$	730.(200) MeV	—
$B^* - B$	29.(5) MeV	45.78(35) MeV
$B_s^* - B_s$	28.5(31) MeV	47.0(26) MeV
$B_2^* - B_0^*$	0 – 250 MeV	—
$B_{s2}^* - B_{s0}^*$	0 – 250 MeV	—

TABLE XXIX. Meson masses and splittings in the D system for $\beta = 5.7$. Overlines denote spin-averaged states.

Splitting	Value	Uncertainties						Experiment
		stat	chiral	strange	shift	a-stat	a-chiral	
$D_s - D$	99.9 MeV	(13)	$(^{+62}_{-0})$	$(^{+234}_{-0})$	(8)	(14)	$(^{+69}_{-0})$	99.2(5) MeV
$D_s^* - D^*$	92.2 MeV	(23)	$(^{+40}_{-0})$	$(^{+218}_{-0})$	(1)	(10)	$(^{+50}_{-0})$	102.4(9) MeV
$\bar{D}_s - \bar{D}$	94.1 MeV	(20)	$(^{+44}_{-0})$	$(^{+222}_{-0})$	(2)	(11)	$(^{+53}_{-0})$	101.6(8) MeV
$D^*(2S) - D^*(1S)$	—	—	—	—	—	—	—	629.(2)(6) MeV [6]
$D_s(2S) - D_s(1S)$	665. MeV	(130)	—	—	(5)	(9)	$(^{+45}_{-0})$	—
$D_s^*(2S) - D_s^*(1S)$	640. MeV	(80)	—	—	(9)	(11)	$(^{+54}_{-0})$	—
$\bar{D}_s(2S) - \bar{D}_s(1S)$	645. MeV	(100)	—	—	(8)	(11)	$(^{+51}_{-0})$	—
$\bar{D}_s^{**}(j_l = \frac{3}{2}) - \bar{D}_s$	—	—	—	—	—	—	—	483.(1) MeV
$\bar{D}_s(1P) - \bar{D}_s(1S)$	411. MeV	(61)	—	—	(3)	(4)	$(^{+27}_{-0})$	—
$\bar{D}_s(2P) - \bar{D}_s(1P)$	710. MeV	(230)	—	—	(7)	(7)	$(^{+36}_{-0})$	—
$D^* - D$	110. MeV	(3)	$(^{+3}_{-0})$	—	(6)	(5)	$(^{+22}_{-0})$	140.64(10) MeV
$D_s^* - D_s$	103. MeV	(2)	—	$(^{+0}_{-2})$	(6)	(4)	$(^{+20}_{-0})$	143.8(4) MeV

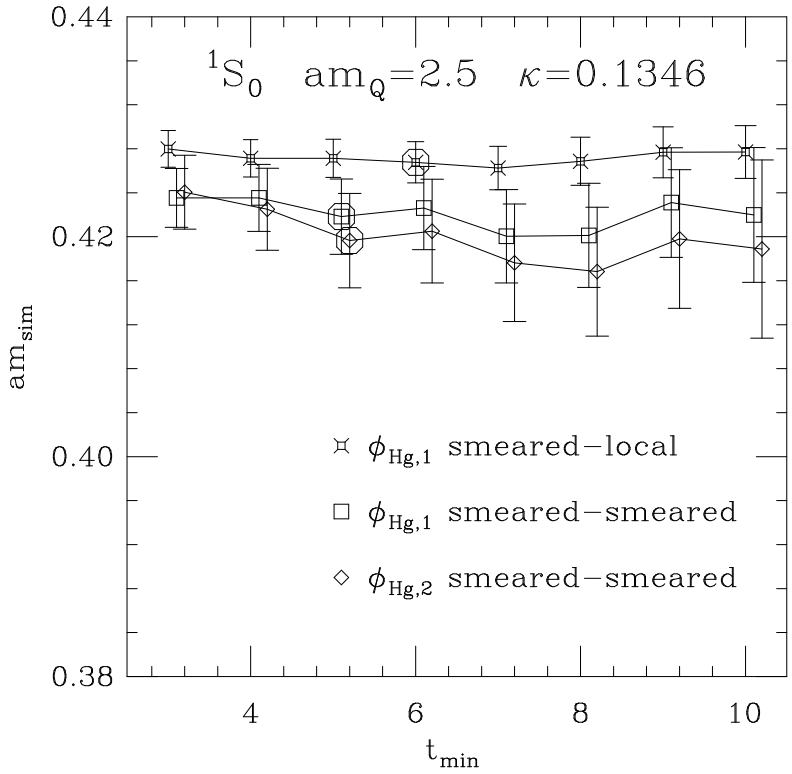

FIG. 1. Dependence of the fitted pseudo-scalar simulation mass on the starting point t_{min} of the fit range at $\beta = 6.2$. The results are shown for three different propagators with smearing at source and sink or at the source only. The octagons give those values of t_{min} which, we determined in the Q-value analysis, to give the final result. The connecting lines are for guidance only.

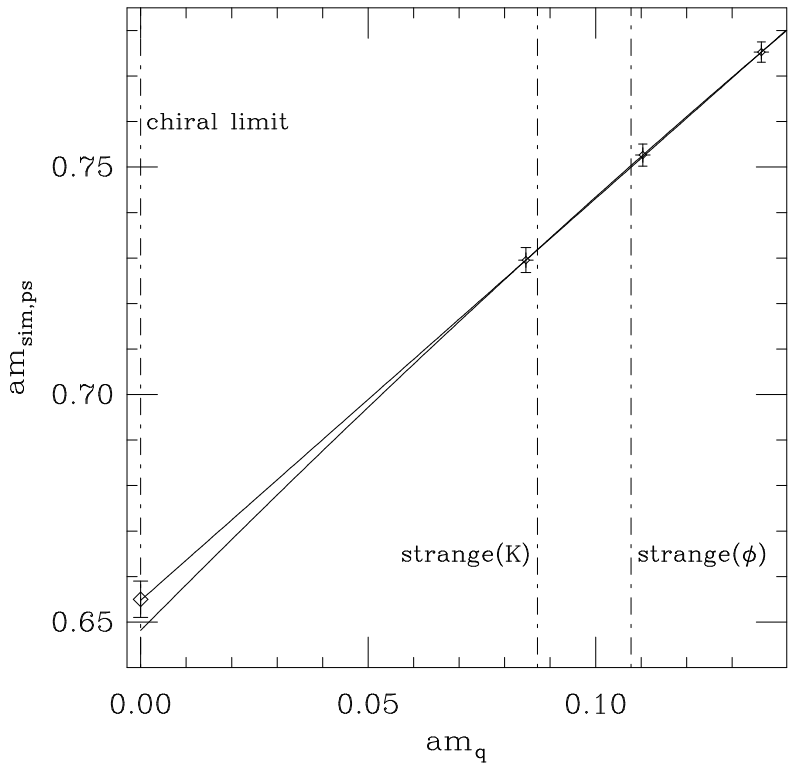

FIG. 2. Chiral extrapolation of the pseudo-scalar simulation mass for $\beta = 5.7$, $a m_Q = 4.0$ in $a m_q = \frac{1}{2}(\frac{1}{\kappa} - \frac{1}{\kappa_c})$. Small symbols give the simulation result. The curves give a linear and quadratic extrapolation as described in the text. The diamond to the left gives the outcome from the linear extrapolation.

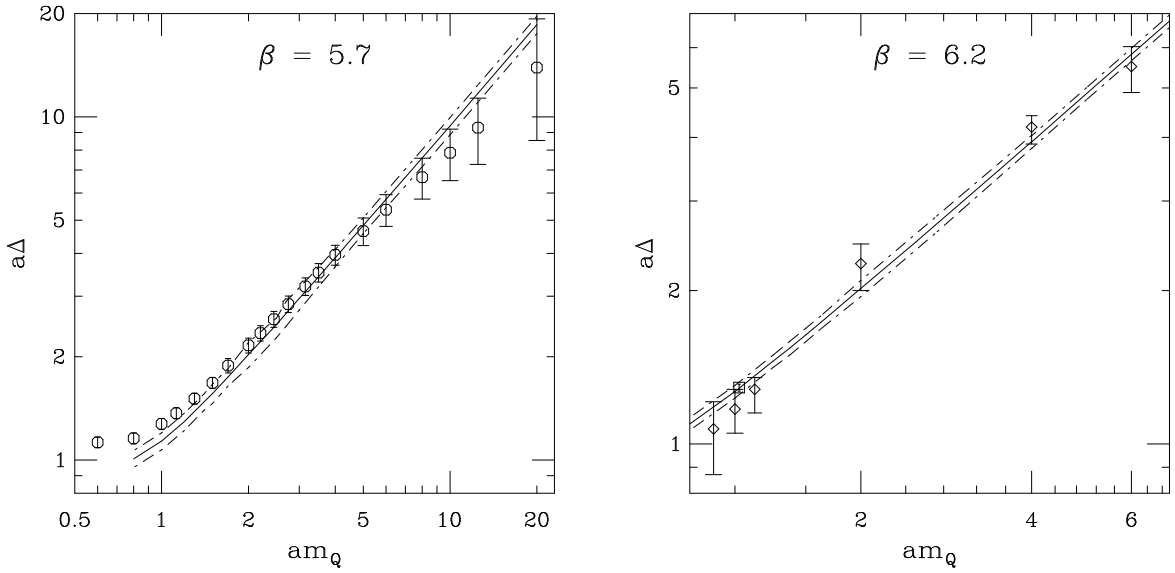

FIG. 3. Comparison of the mass shift $a\Delta$ from the simulation and lattice perturbation theory as a function of the bare heavy quark mass am_Q. The octagons give the outcome of the dispersion relation for heavy light mesons, diamonds from heavyonium. The lines represents the perturbative outcome. The square gives the heavyonium shift from reference [29] for $\beta = 6.2$ for comparison.

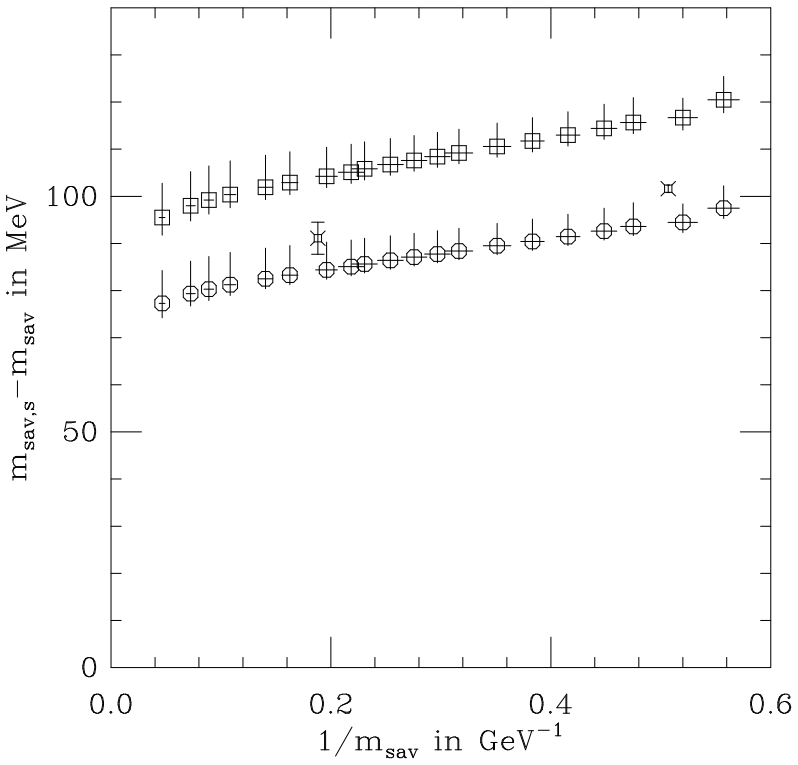

FIG. 4. Mass splitting between the spin-averaged ground state S-wave heavy-light strange and non-strange meson. The octagons give the result for κ_s determined from the K-meson, squares from the ϕ-meson. For both data sets the upper errors give the uncertainty from the different chiral extrapolations, the lower ones the statistical uncertainty. For simplicity this figures does not consider uncertainties arising from the value of a, see eq. (5a). Experimental results are displayed by the fancy squares.

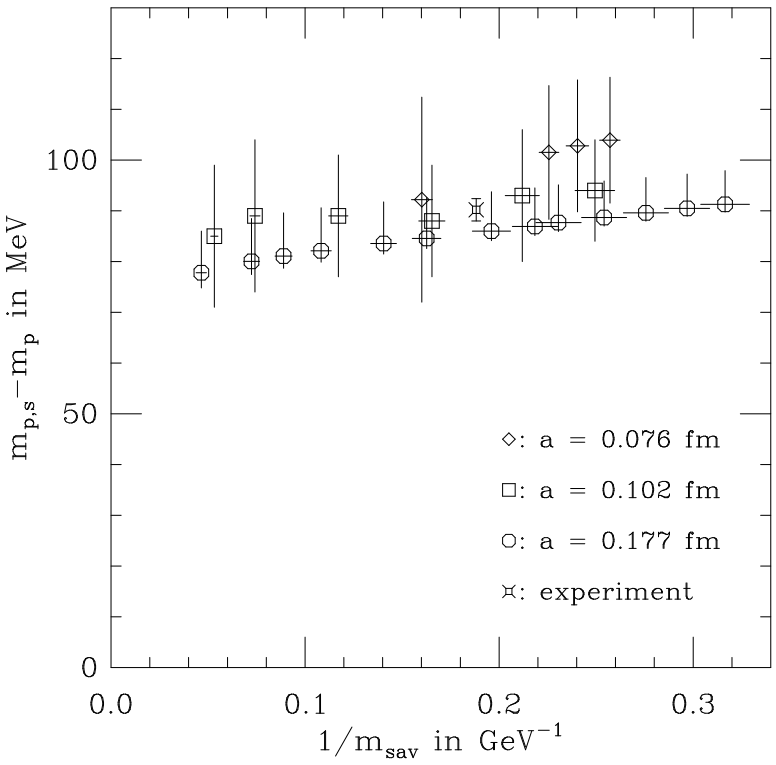

FIG. 5. Comparison of the strange non-strange splitting for the pseudo-scalar state at different values of the lattice spacing a. Octagons give our result for $\beta = 5.7$ and diamonds for $\beta = 6.2$. The squares give the result from [12] at $\beta = 6.0$ and the fancy square the experimental outcome for the B-meson [3]. For $a = 0.102$ fm and 0.076 fm we give the statistical errors only, the errors for $a = 0.177$ fm have been described in figure 4.

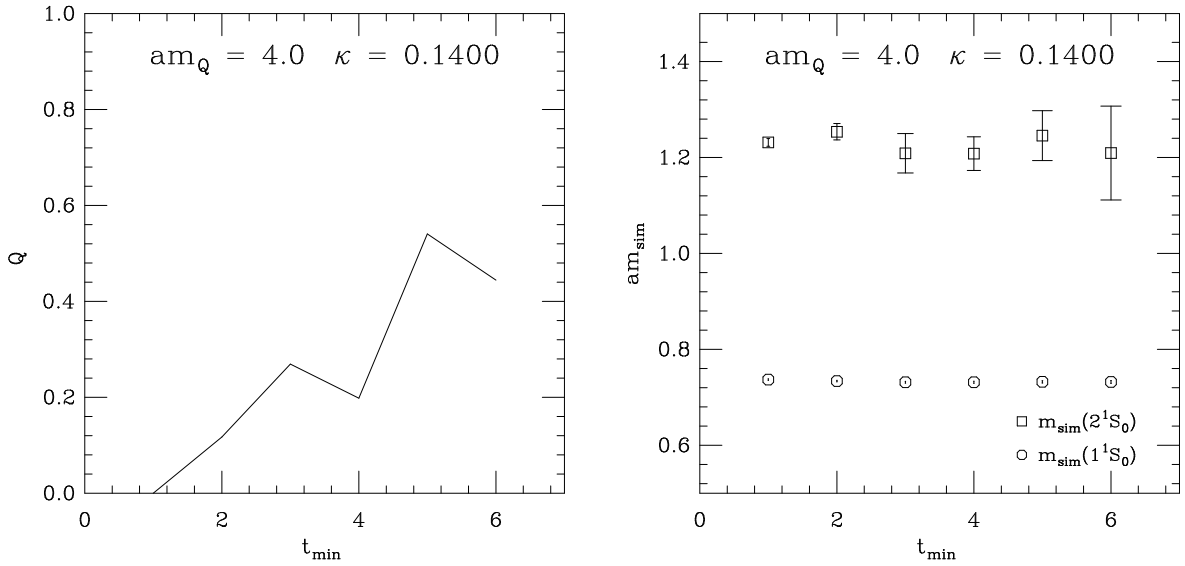

FIG. 6. Fitting the radially excited S-state at $\beta = 5.7$. The left hand side gives the Q-values and right hand side the fitted simulation masses of the pseudo-scalar ground state and the first radially excited state.

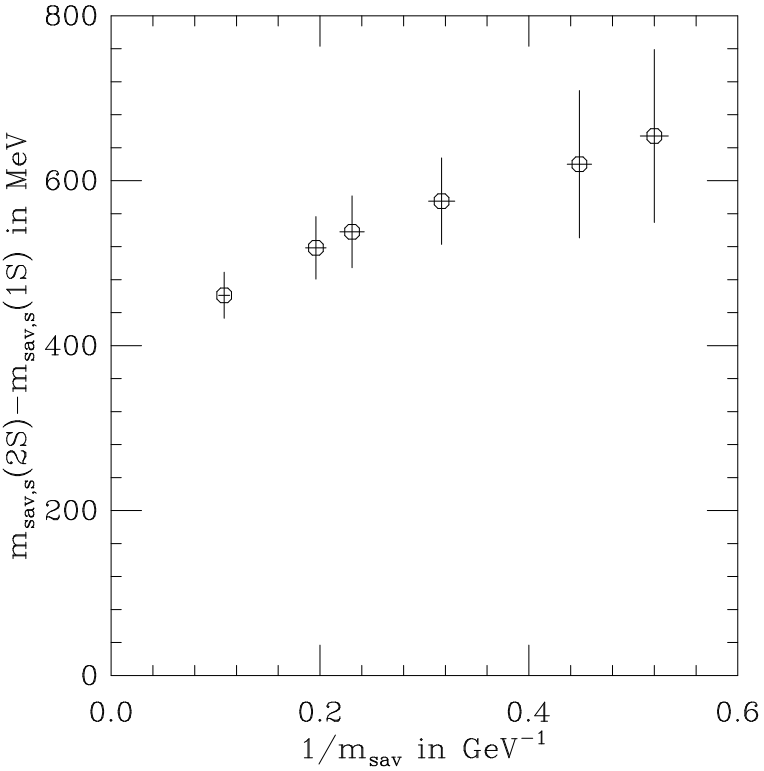

FIG. 7. Splitting between radially excited and ground state S-wave splitting at $\beta = 5.7$. The results are for $\kappa = 0.1400 \approx \kappa_s(K)$ and the spin-average.

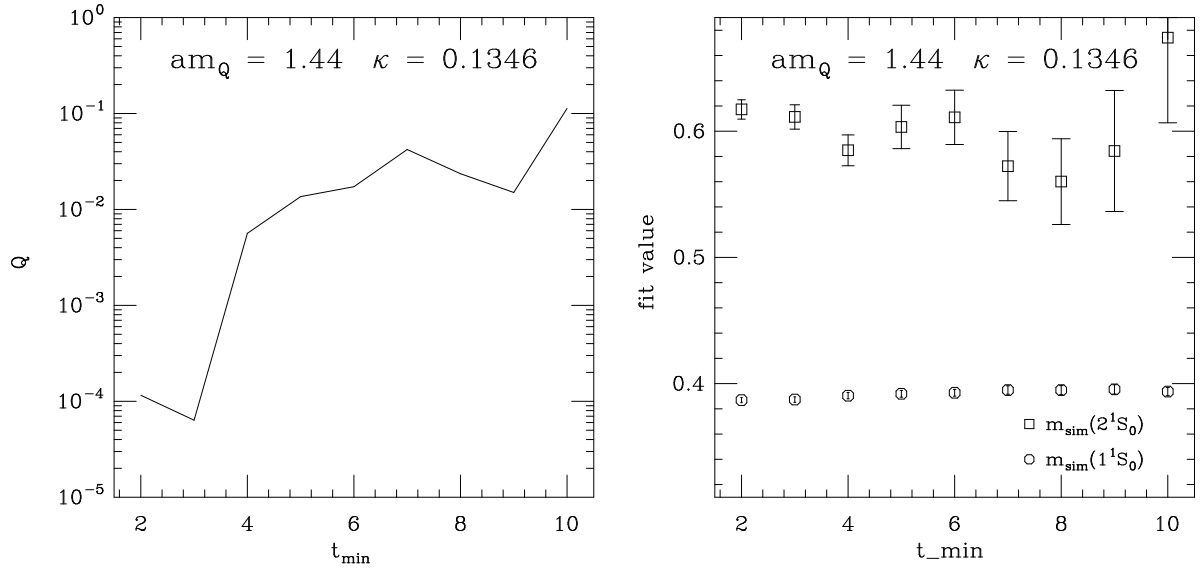

FIG. 8. Fitting the 2*S* radial excitation at $\beta = 6.2$. Again we give the Q-values and on the right the simulation masses of the pseudo-scalar ground state and the first radially excited state. This example uses $\phi_{\mathrm{Hg},1}$ and $\phi_{\mathrm{He},1}$ at the sources.

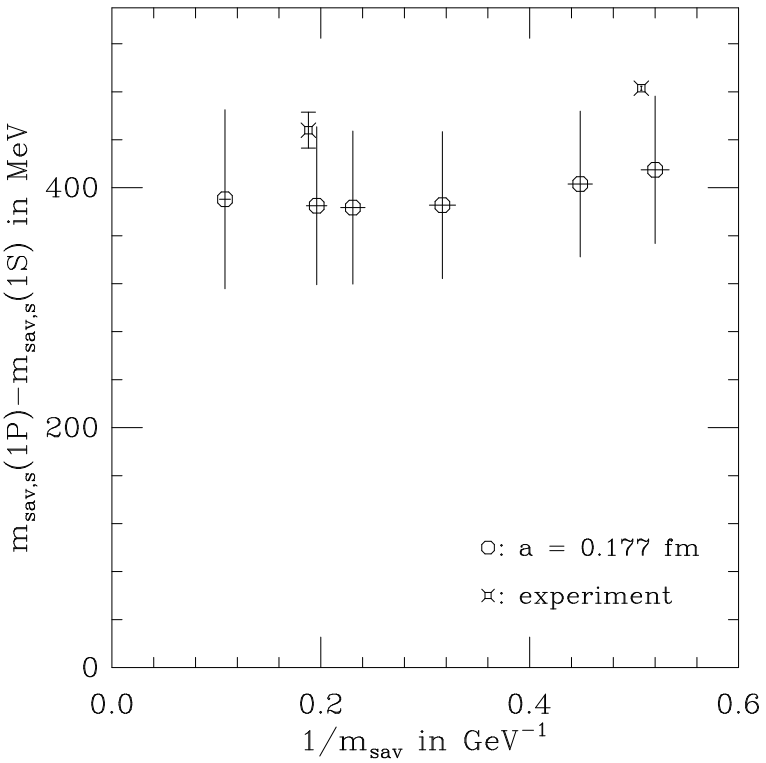

FIG. 9. Splitting of spin-averaged P to S-wave. The results are for strange light quarks and the error bars give the statistical uncertainties only. The experimental result gives the $B^*_{sJ}(5850)$ resonance and the spin-average of the D_{s1} and D^*_{s2}.

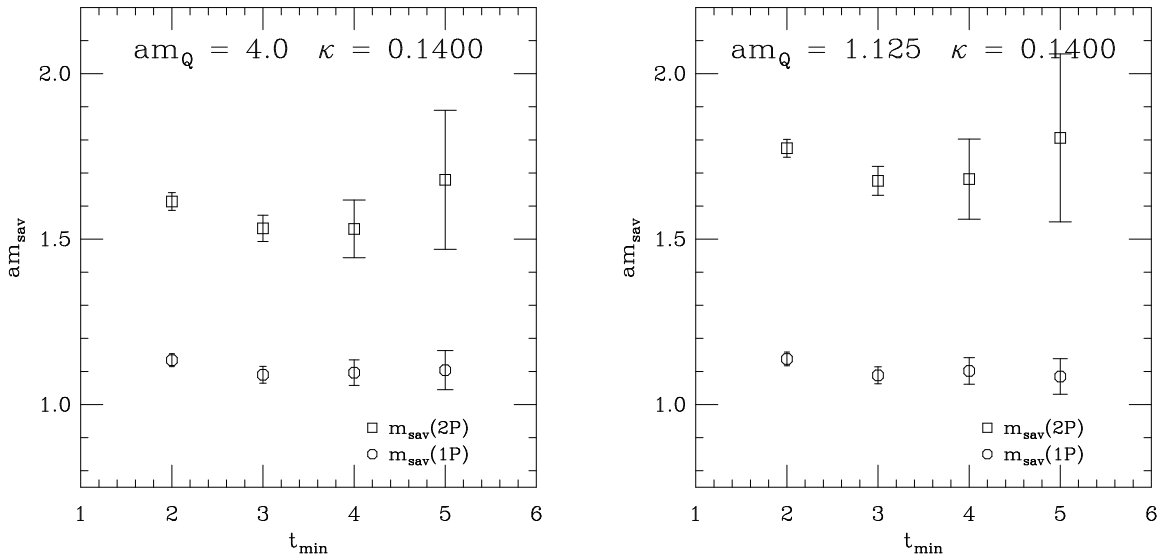

FIG. 10. Fitting radially excited P-states at $\beta = 5.7$. The plots give the spin-averaged 1P and 2P states. The final answer is extracted from $t_{min} = 5$ in both cases.

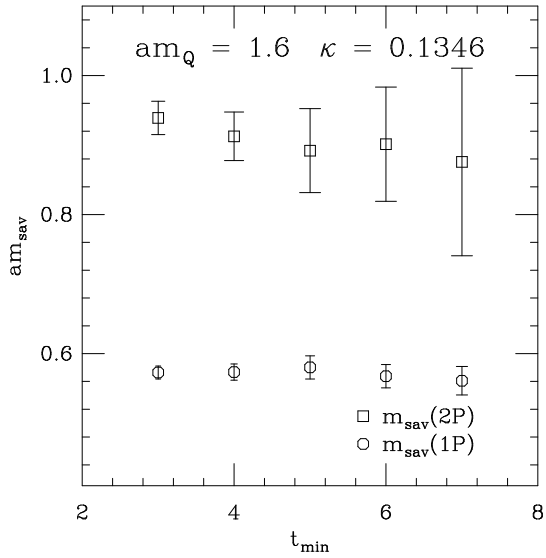

FIG. 11. Fitting radially excited P-states at $\beta = 6.2$. The plots give the spin-averaged 1P and 2P state. We take our final result from $t_{min} = 6$.

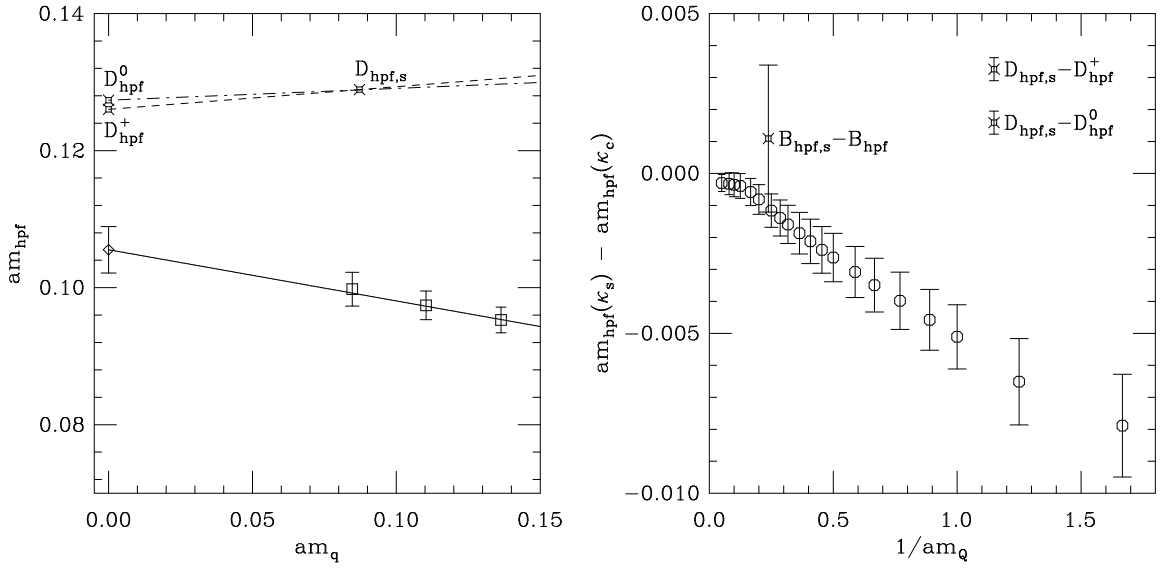

FIG. 12. Light quark mass dependence of the hyperfine splitting at $\beta = 5.7$. On the left hand side we show a linear fit to all 3 data points for $am_Q = 0.8$. This corresponds approximately to the D meson. The fancy squares give the experimental result. The right hand side gives the fitted slope multiplied by am_s, as determined from the K, for all m_Q. In order not to disguise the significance of our findings, the error bar gives the statistical errors of the fit parameter only. Experimental results are given by the fancy squares.

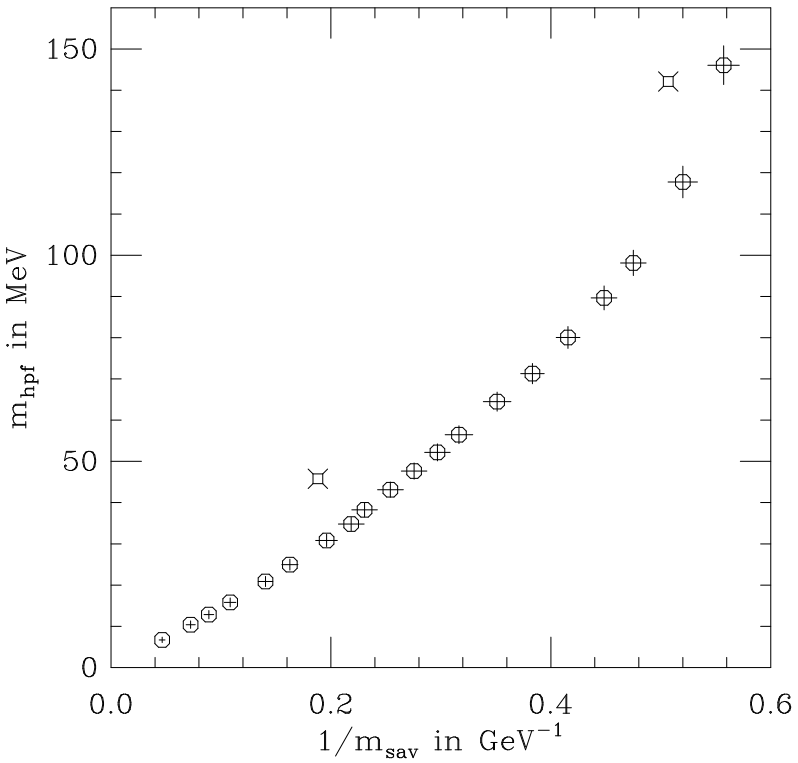

FIG. 13. The hyperfine splitting as a function of the spin-averaged heavy-light meson mass. Error bars give statistical uncertainties only. The fancy squares give the experimental result [3].

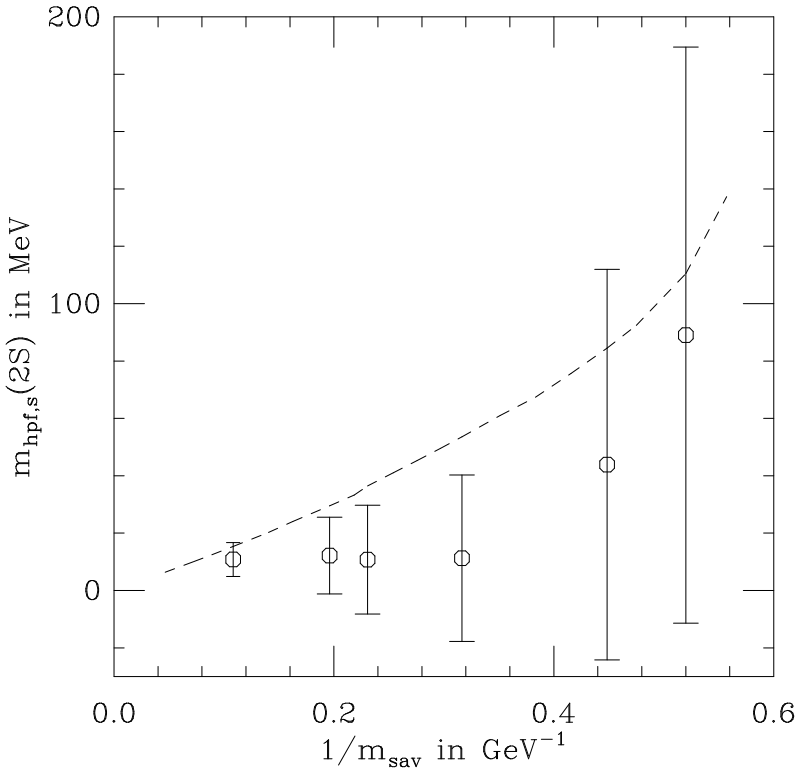

FIG. 14. The hyperfine splitting of the radially excited S-wave state is given by the octagons. The error bars give statistical uncertainties only. The dashed line gives the ground state hyperfine splitting of the strange meson for comparison. This line is not a fitted curve.

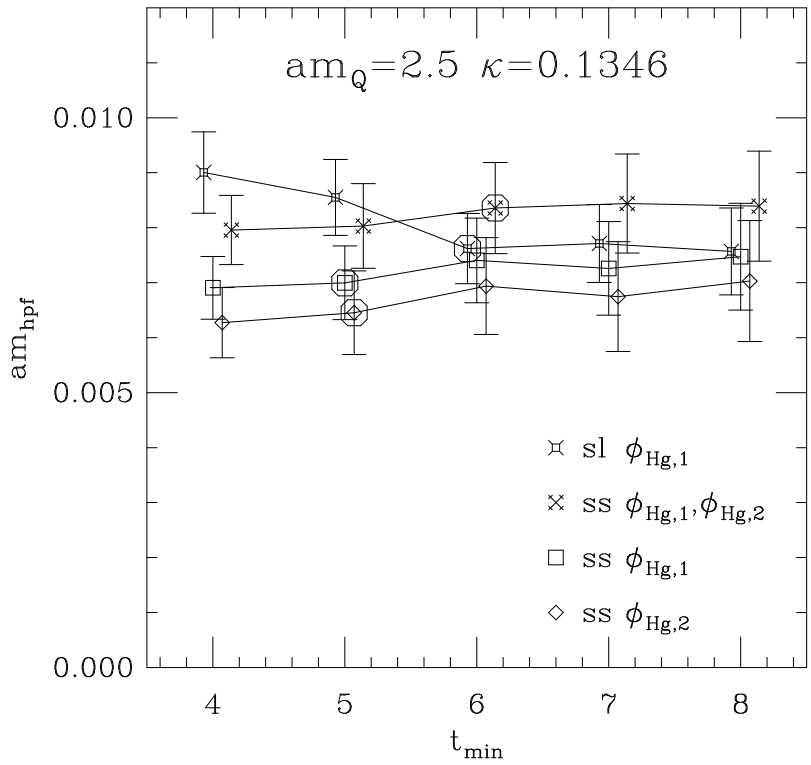

FIG. 15. Hyperfine splitting in the N run at $\beta = 6.2$. The results are extracted from the difference of fitted masses for the $^3S_1$ and $^1S_0$ propagators. We display the dependence on the starting point t_{min} of the fit range of the propagators. In all cases we used single exponential fits. With 'sl' we denote results obtained from smeared-local propagators, 'ss' refers to smearing at source and sink. The octagons give those t_{min}, which we determined in the Q-value analysis to give the final result. The connecting lines are for guidance only.

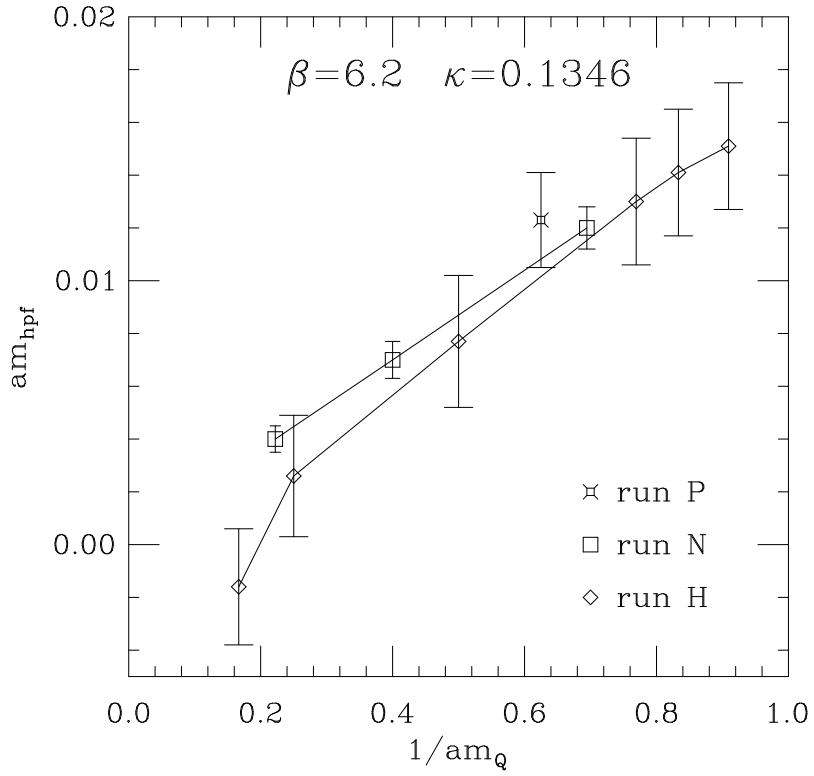

FIG. 16. Comparison of the outcome for the hyperfine splitting from the different runs at $\beta = 6.2$. The lines are for guidance only and connect the points of the different runs.

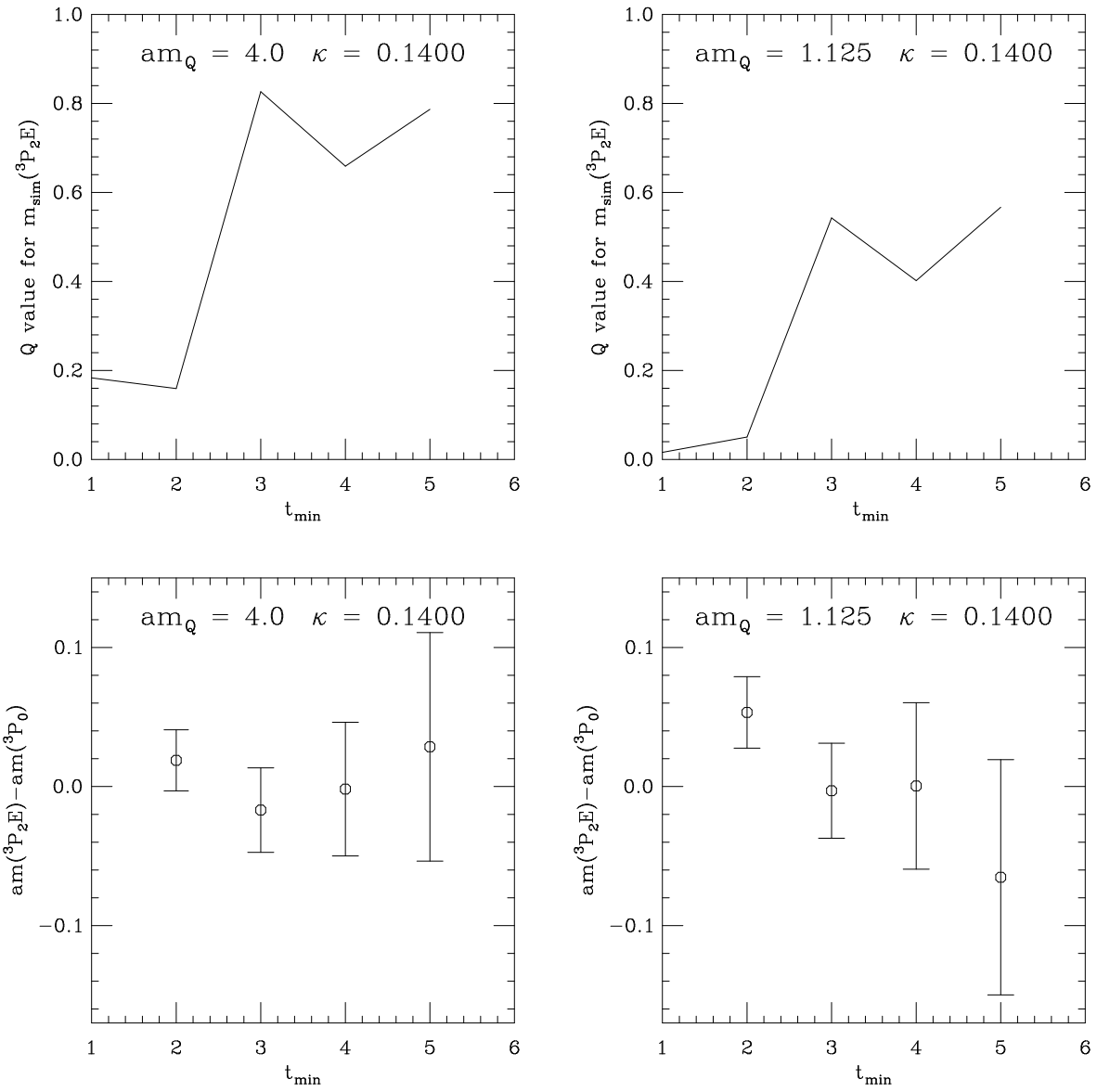

FIG. 17. Fit range dependence of the $m(^3P_2E) - m(^3P_0)$ P-state fine structure from a double exponential matrix fit at $\beta = 5.7$. The upper line displays the Q-value of the fit to the ^3P_2E-state. The fit to the $^3P_0$-state gives $Q > 0.6$ even for $t_{min} = 1$. The bottom line gives the splitting as determined from the difference of the individual fit results.

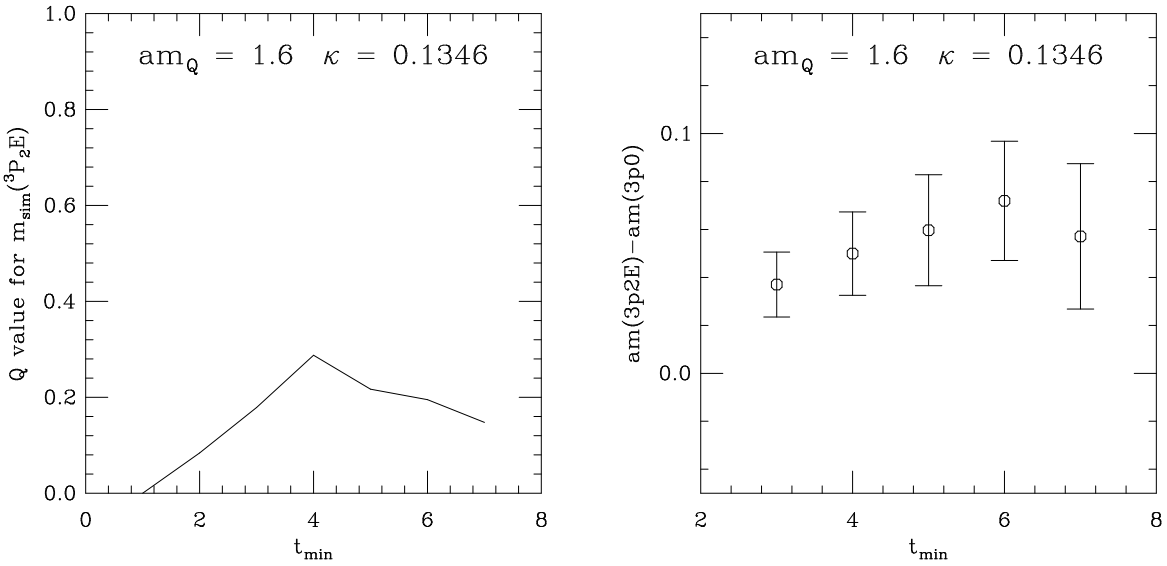

FIG. 18. Fit range dependence of the $m(^3P_2E) - m(^3P_0)$ P-state fine structure from the double exponential vector fit at $\beta = 6.2$. The left hand side displays the Q-value of the fit to the ^3P_2E-state. The fit to the $^3P_0$-state gives even higher Q-values. The right hand side gives the splitting as determined from the difference of the individual fit results.

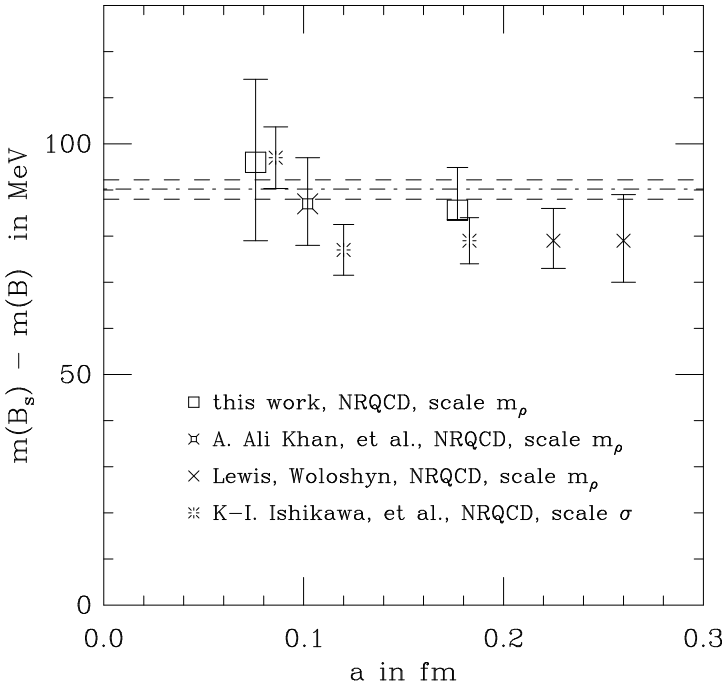

FIG. 19. Compilation of results for the $B_s - B$ splitting. Additional results are from [12,34,35]. Results are for κ_s fixed from K/ρ ratio, apart from the crosses. The latter use the K^*/K ratio to fix κ_s, which tends to shift them downwards. Please note the bursts and crosses do not contain all sources of uncertainty included in the squares and fancy squares. The horizontal lines give the experimental result from [3].

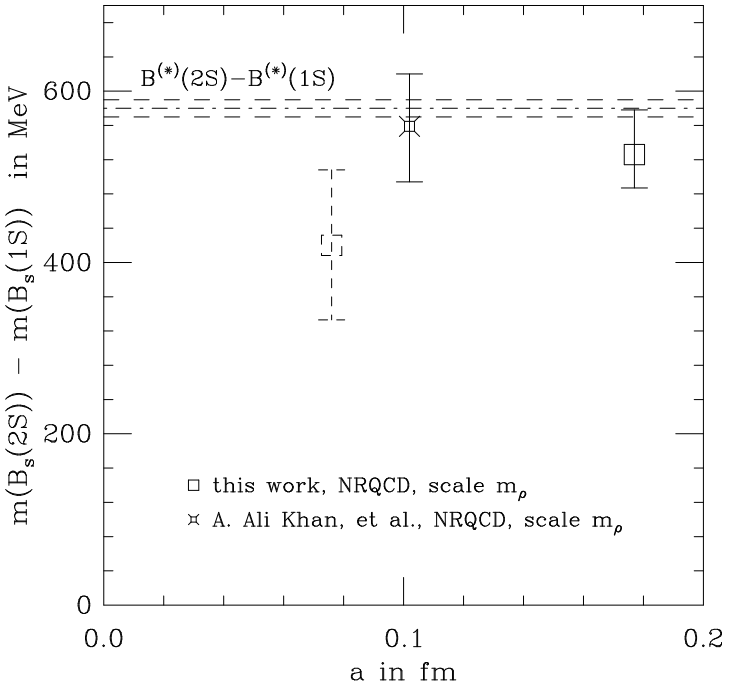

FIG. 20. Scaling of the $B_s' - B_s$ splitting. The squares give our results and the fancy square the one from [12]. On our finest lattice the extraction of the result turned out to be substantially more difficult than elsewhere, so we give this result with dashed lines, see text. The horizontal lines give a preliminary experimental result for an admixture of the non-strange $B' - B$ and $B^{*\prime} - B^*$ splitting from the DELPHI-collaboration [4,5] for comparison.

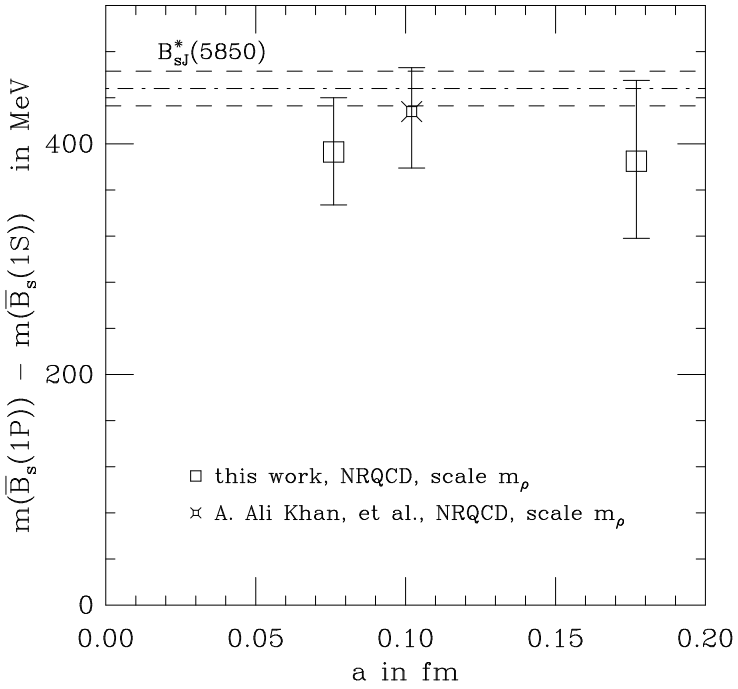

FIG. 21. Scaling of the spin-averaged $\bar{B}_s(1P) - \bar{B}_s(1S)$ splitting. We include the result of [12]. The horizontal lines give the $B^*_{sJ}(5850)$ resonance, which is expected to be a superposition of the two $j_l = \frac{3}{2}$ states.

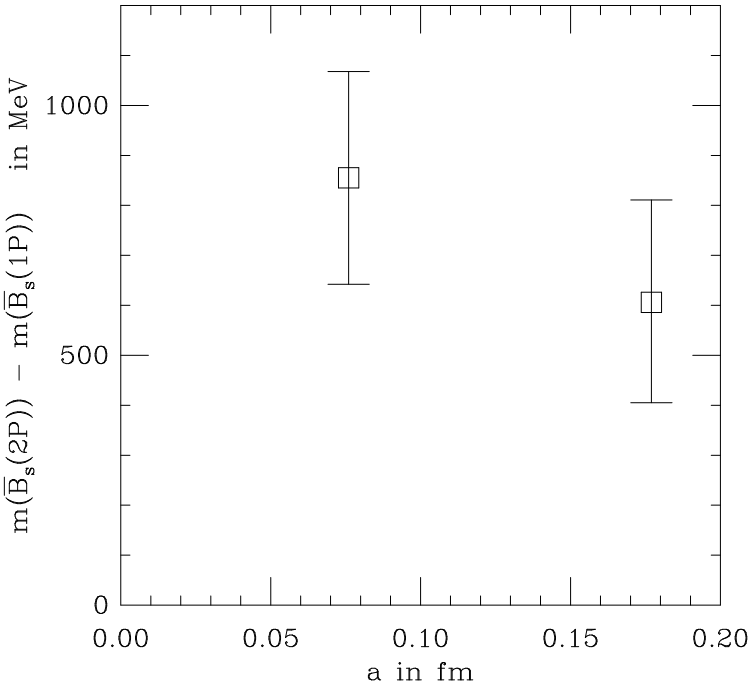

FIG. 22. The spin-averaged $\bar{\mathsf{B}}_s(2\mathsf{P}) - \bar{\mathsf{B}}_s(1\mathsf{P})$ splitting for two different values of the lattice spacing $\mathfrak{a}$.

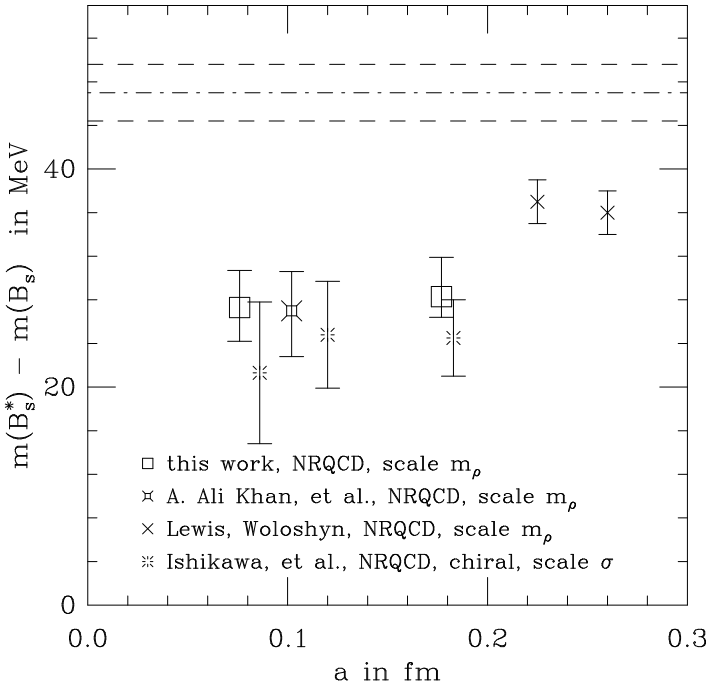

FIG. 23. Results for the hyperfine splitting $B_s^* - B_s$ for different a-values. Results from [12,34,35] are included into the plot. The bursts give results for the chirally extrapolated $B^* - B$ splitting. Their error bar gives only statistical errors. Crosses omit the uncertainties from the determination of the bare b-mass. The horizontal lines give the experimental result from [3].

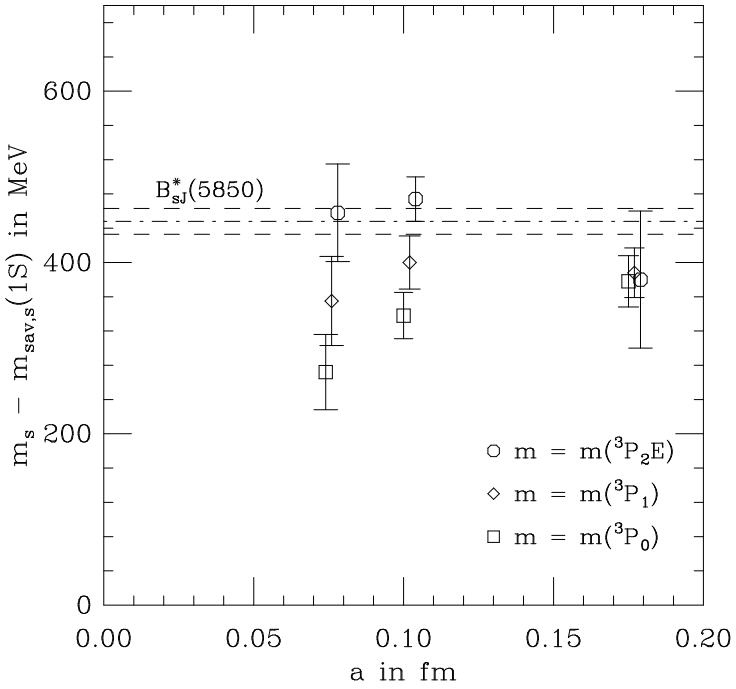

FIG. 24. Scaling of the P-state fine structure of the B_s. Results at $a = 0.102$ fm are from [12]. The squares and octagons are displaced for clarity.

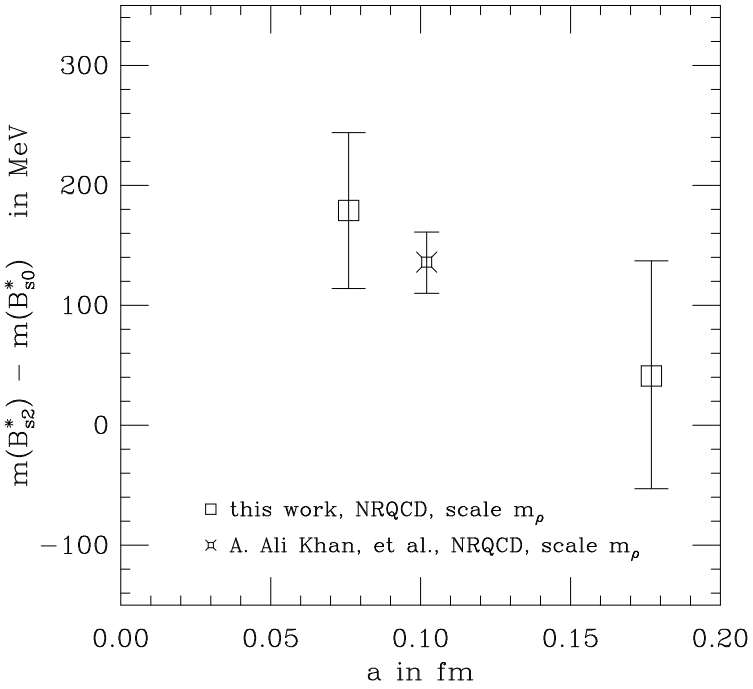

FIG. 25. Results for the P-state fine structure $B^*_{s2} - B^*_{s0}$ for three different a-values. The middle point has been taken from [12]. Experimentally this splitting is so far unobserved.

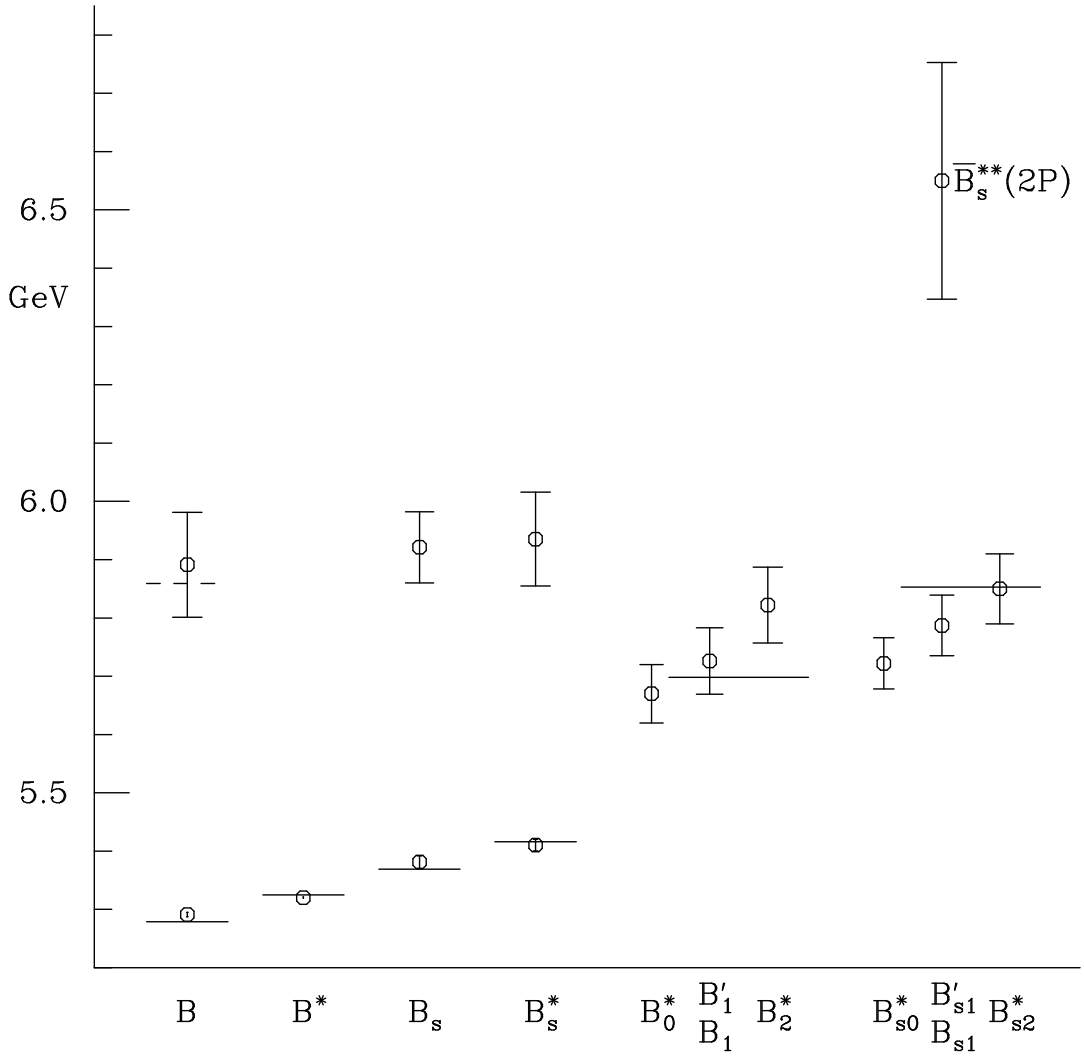

FIG. 26. Spectrum of B-mesons, summarising our results and those of [12]. As before, the lattice results, given by the octagons, give the splitting with respect to the spin-averaged 1S-state $\bar{\mathrm{B}}$. The experimental results from [3] are included by horizontal lines. The dashed line displays a result from the DELPHI collaboration [4,5], interpreted to be the $\mathrm{B}^{(*)\prime}$. The P states are compared to the experimental result for the $\mathrm{B}_{\mathrm{J}}^*(5732)$ and $\mathrm{B}_{\mathrm{sJ}}^*(5850)$.

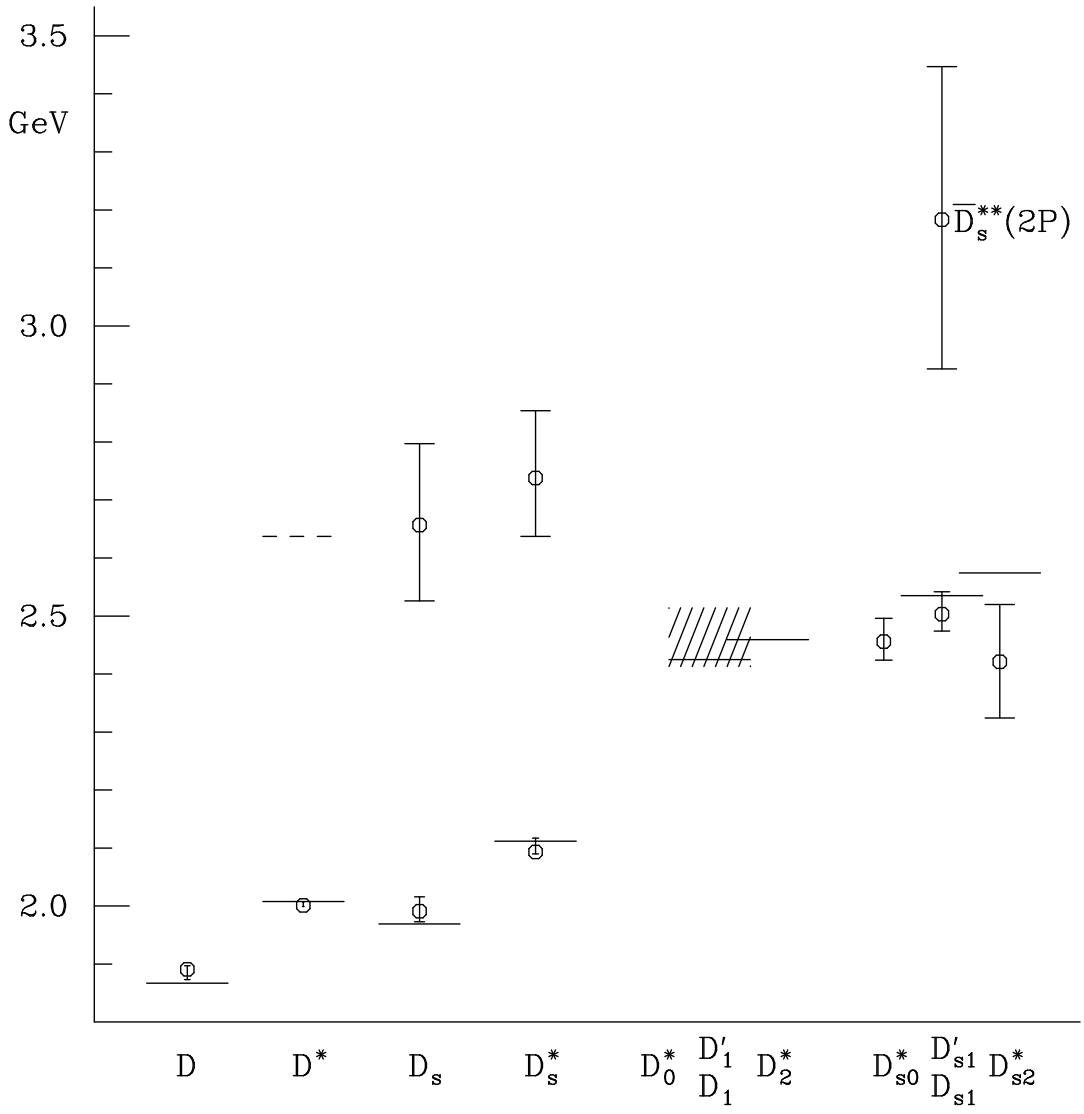

FIG. 27. Spectrum of D-mesons from our results at $\beta = 5.7$. Lattice results are given by octagons, experimental results from [3] by horizontal lines. The lattice results give the splitting with respect to the spin-average $\bar{D}$ of the 1S-wave. The dashed line displays a result from the DELPHI collaboration [6], interpreted to be the $D^{*\prime}$. There are two non-degenerate P-states with J^P quantum numbers 1^+ corresponding to the $j_l = \frac{1}{2}$ and $\frac{3}{2}$ state. We denote these by D_1 and D_1' respectively and similarly for the D_s. The CLEO collaboration reported preliminary results for the D_1 corresponding to $j_l = \frac{1}{2}$ [7,8]. The shaded area gives this result.

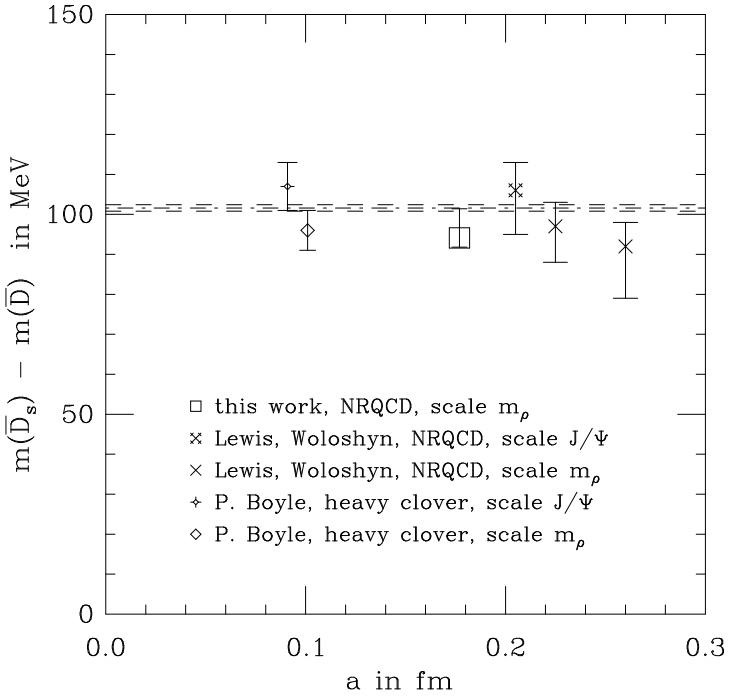

FIG. 28. Comparison of recent lattice results for the strange to non-strange splitting for the spin-average of the D and D^*-mesons. The square and both of the diamonds [38] use the K/ρ mass-ratio to fix κ_s, whereas the crosses [34] use the K^*/K ratio. The horizontal line gives the experimental result from [3].

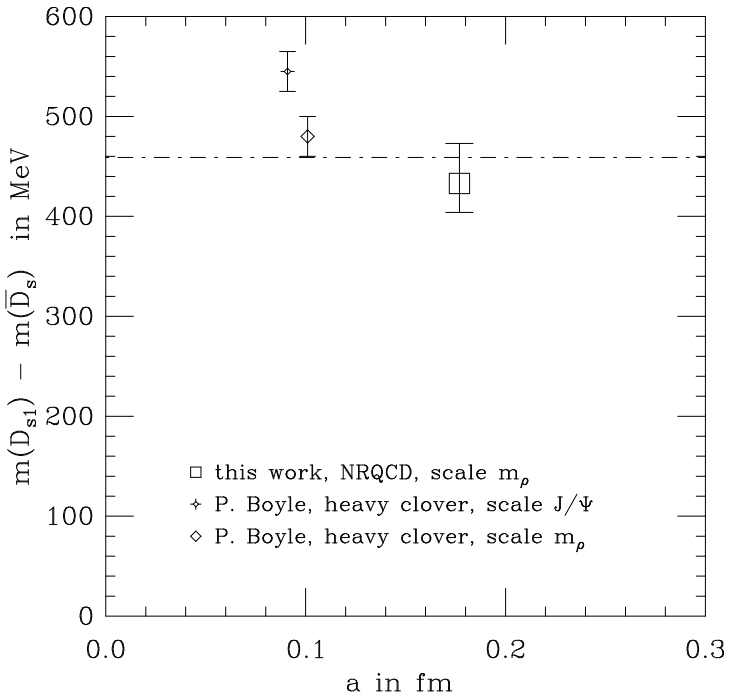

FIG. 29. Comparison of the $D_{s1} - \bar{D}_s$ to the result of [38]. The experimental result for the D_{s1} is again from [3].

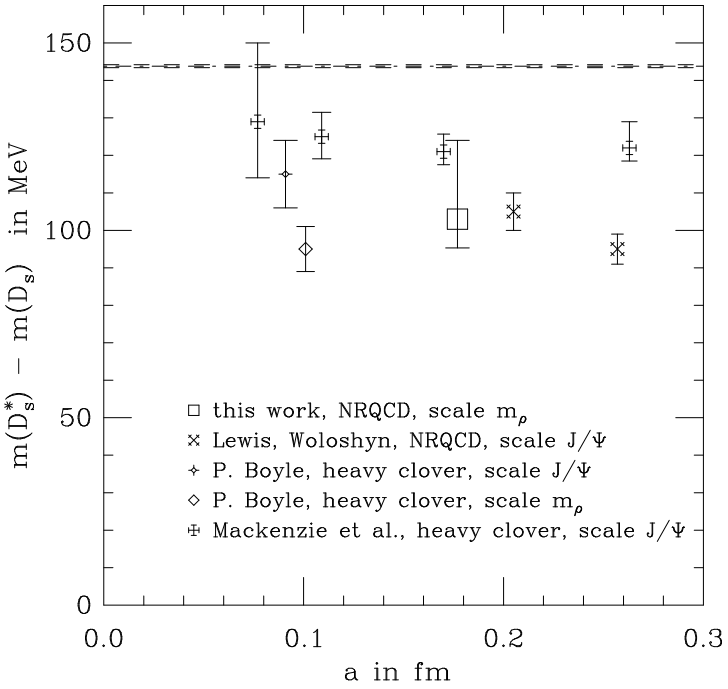

FIG. 30. Comparison of our D_s-meson hyperfine splitting to the findings of [34,38,39]. Please note that these other results do not necessarily include all the sources of uncertainty, that we have included, see table XXIX. They therefore may have underestimated error bars. Again, we quote the experimental result from [3]. See text for a discussion.